Journal of Petroleum Science and Engineering 195 (2020) 107725

Contents lists available at ScienceDirect

Journal of Petroleum Science and Engineering

journal homepage: http://www.elsevier.com/locate/petrol

Development of an embedded discrete fracture model for 2D and 3D unstructured grids using an element-based finite volume method

Y. Xu [a,*], I.C.M. Lima [b], F. Marcondes [b], K. Sepehrnoori [a]

[a] The University of Texas at Austin, USA
[b] Federal University of Ceará, USA

ARTICLE INFO

Keywords:
Embedded discrete fracture model
2D unstructured grid
3D unstructured grid
Element-based finite volume method
Mixed elements
Fractured reservoir

ABSTRACT

Recently, the unstructured gridding technique has been extensively used in reservoir simulation because of the high flexibility it provides to represent geologically realistic reservoirs. The embedded discrete fracture model (EDFM) has also attracted attention in recent years for the simulation of complex fractures in various types of computational grids. In this work, we develop a methodology to apply the EDFM in 2D and 3D unstructured grids using an element-based finite volume method (EbFVM). In this method, triangular and quadrilateral elements are used in 2D grids, and tetrahedron, prism, hexahedron, and pyramid elements are used in 3D grids. New approaches to addressing matrix-fracture connectivity and reducing the number of fracture unknowns in this type of grid are presented. The methodology is implemented in an EDFM preprocessing code.

A series of case studies are presented to demonstrate the methodology in 2D and 3D simulations using an in-house compositional reservoir simulator. Different types of elements are used in the simulations to represent the reservoir geometries. Both primary and secondary recovery processes are simulated. The results show that when the number of control volumes is similar, the proposed method can obtain similar results on different grids with various types of elements, which confirms the effectiveness of the approach. Case studies with complex reservoir geometries are also presented to demonstrate the applicability of the model.

This work demonstrates the extensiveness of the EDFM to unstructured matrix grids. It also shows the compatibility of the EDFM with various numerical approximation schemes. The use of unstructured gridding with mixed types of elements facilitates the representation of complex reservoir geometries, and through the combination with the EDFM, complicated gridding around fractures is avoided. Therefore, the approach in this work has high flexibility for simulating densely fractured media with complex geometries.

1. Introduction

Unstructured grids have been used in reservoir simulation to represent geologically complex reservoirs (Fung et al., 1992; Durlofsky and Chien, 1993; Verma and Aziz, 1997; Prévost et al., 2002, 2005; Edwards, 2002; Hoteit and Firoozabadi, 2006a; Vitel and Souche, 2007; Marcondes and Sepehrnoori, 2007, 2010; Araújo et al., 2016; Fernandes et al. 2016, 2017; Samier and Masson, 2017). In comparison with structured grids, unstructured grids are more capable of representing irregular reservoir structures and reservoir boundaries, as they provide more flexibility regarding the geometry of gridblocks and their discretization.

There are several types of numerical approximation schemes used for unstructured grids, including the finite volume method (Fung et al., 1992; Edwards, 2002; Marcondes et al., 2013; Fernandes et al., 2017), finite element method, and mixed finite element method (Durlofsky and Chien, 1993; Hoteit and Firoozabadi, 2006). The control-volume finite element method (CVFEM) (Baliga and Patankar, 1980; Forsyth, 1990; Fung et al., 1992) is also a widely used numerical approximation scheme for unstructured grids. It was initially proposed for solving Navier-Stokes flow in computational fluid dynamics (Baliga and Patankar, 1980). This method borrows the concepts of elements and shape functions from the finite element method. The computational grids used in this method are defined as a series of elements. Physical properties such as pressure, phase saturations, and number of moles of each component are evaluated at the vertices of the elements, and porosity and permeability are stored on the elements. As a combination of the finite element method and the finite volume method, the CVFEM

* Corresponding author.
E-mail address: yifei.xu@utexas.edu (Y. Xu).

https://doi.org/10.1016/j.petrol.2020.107725
Received 30 September 2019; Received in revised form 2 June 2020; Accepted 30 July 2020
Available online 14 August 2020

maintains the high flexibility in terms of discretization in the finite element method, and it keeps the local mass conservation in the finite volume method. Another advantage of this method is that it can be easily implemented in simulators with the capability to construct arbitrary connections between cells (Forsyth, 1990). Because the CVFEM still uses a finite volume formulation, it is also called the element-based finite volume method (EbFVM) (Maliska, 2004; Cordazzo et al., 2005; Marcondes and Sepehrnoori, 2007), which better reflects its nature. Therefore, in the remainder of this paper, this method will be referred to as EbFVM.

Similar to corner-point grids, unstructured grids have the capability to explicitly represent certain geological features, such as fractures, by creating conforming meshes honoring the geological features (Noorishad and Mehran, 1982; Karimi-Fard et al., 2004; Matthai et al., 2005; Karimi-Fard and Durlofsky, 2016; Zidane and Firoozabadi, 2018; Hui et al., 2018). However, as the number and complexity of fractures increase, it can be time-consuming and sometimes extremely challenging to generate the desired mesh. Other issues involve the large number of gridblocks due to the discretization around fractures and the large linear system of equations. These issues can be solved to a certain extent by using non-conforming meshes to simulate fractures, which can be achieved by combining the usage of unstructured grids with certain discrete fracture modeling techniques, such as the EDFM.

The EDFM uses non-conforming meshes to avoid the complex matrix gridding around an arbitrary fracture geometry. In the EDFM, the matrix gridding is generated regardless of the geometry of fractures, thus keeping the grid generation process relatively simple. For example, regular Cartesian grids can be readily used. The fractures are represented in a separate domain that is connected to the matrix domain through special connections. The basic idea and formulations of the EDFM have been proposed and extended by several researchers (Hearn et al., 1997; Lee et al., 2001; Philip et al., 2005; Li and Lee, 2008; Moinfar et al., 2014). Extensive previous studies have also shown the high reliability and computational efficiency of the model (Moinfar et al., 2014; Panfili et al., 2015; Xu et al., 2017; Du et al., 2017; Flemisch et al., 2018). For example, Panfili et al. (2015) compared the EDFM with the local grid refinement method and the equivalent fractured well method, and in their study, the EDFM obtained a higher computational efficiency compared with the local grid refinement method. Du et al. (2017) compared the EDFM with an unstructured gridding fracture model for full-field well interference studies, and the EDFM was found to have a significant advantage regarding computational efficiency while maintaining high accuracy. Flemisch et al. (2018) did a benchmark study comparing the EDFM with six discrete fracture models (DFMs) based on unstructured grids or the extended finite element method (XFEM). The results of the EDFM showed good agreement with other models.

Besides simulating high-permeability fractures, some researchers have proposed methods to use the EDFM to handle fractures that act as flow barriers. Tene et al. (2017) and Jiang and Younis (2017) projected the fracture to the closest interfaces of the matrix gridblock and modified the transmissibility between the fracture and matrix to decrease the fluxes when the permeability of the fracture is low. This approach was called projected EDFM (pEDFM). Chai et al. (2018) presented another method called compartmental EDFM (cEDFM) to deal with flow barriers. In this approach, whenever a discrete fracture crosses a matrix gridblock, it splits the matrix gridblock, hence the flows from both parts of the split matrix gridblock to the fracture are treated separately. Similar to the pEDFM, the cEDFM also improved the simulation accuracy for fluid flow near faults.

Besides regular Cartesian grids, the EDFM has been used with other types of matrix grids to combine the flexibility provided by these types of gridding with the advantages of the EDFM. All these studies showed the generality and effectiveness of the EDFM in different types of grids. For example, Jiang and Younis (2016) incorporated the EDFM with the multiple interacting continua (MINC) method. Ding et al. (2018) developed an EDFM-MINC approach where they used a MINC proximity function to subdivide the matrix and calculate matrix-fracture flow exchange. Hui et al. (2019) coupled the EDFM with the dual-porosity dual-permeability model. Panfili and Cominelli (2014), Fumagalli et al. (2016), and Xu and Sepehrnoori (2019) implemented the EDFM in corner-point grids. Panfili et al. (2015) and Yang et al. (2018) demonstrated the use of EDFM with moderate local grid refinement to improve the simulation accuracy of this model.

The use of the EDFM in unstructured grids has not been studied extensively. Fang et al. (2016) combined the EDFM in a triangular mesh with the dual-continuum model to evaluate the transient flow of horizontal wells with complex fracture networks. Norbeck et al. (2016) developed a numerical framework to calculate the coupled processes of fluid flow and geomechanics, where the fluid flow problem was solved with the EDFM in two-dimensional triangular meshes. The use of the EDFM in two-dimensional unstructured grids with mixed elements or in three-dimensional unstructured grids has not been studied by previous researchers. With the increasing use of unstructured gridding in reservoir simulation, it is beneficial to extend the EDFM to such unstructured grids to take full advantage of the flexibility offered by unstructured gridding, including the possibility of using different types of elements in a single grid, and simulate geologically complex fractured reservoirs. Furthermore, to the best of our knowledge, there has not been study on the application of the EDFM in unstructured grids using the EbFVM, although the EbFVM has been a widely used scheme in the area of reservoir simulation. The extension of the EDFM to grids using this scheme can further extend the application of the EDFM and provide valuable insights on the extensibility and applicability of the EDFM. It should be noted that although it is possible to model irregular fractured reservoirs using Cartesian and corner-point grids in conjunction with the use of inactive cells and apply the EDFM in such grids, it is important to have more accurate geometrical tools to discretize complex fractured reservoirs mainly for two important reasons. First, it might be difficult to generate a grid using Cartesian or even corner-point grids for some reservoirs with complex shapes and subsurface features. Second, even though an inactive grid configuration can be found that would be able to model the irregular geometry of the reservoir for a specific structured grid configuration, when we want to perform a grid refinement, all the inactive grid configurations need to be reprocessed. For a very irregular reservoir geometry, this could be a time-consuming task. Therefore, the ability to use the EDFM in conjunction with unstructured grids is important to conveniently simulate fractured reservoirs with complex geometries and subsurface features.

In this work, the EDFM is extended to 2D and 3D unstructured grids (with mixed elements) using the EbFVM to combine the flexibility provided by unstructured gridding with the EDFM and demonstrate the extension of the EDFM to unstructured grids. First, the numerical formulations of the EbFVM are presented. Subsequently, methodology and formulations are developed to apply the EDFM in unstructured grids using the EbFVM, with a focus on the discretization of fractures and the transmissibility calculation between matrix blocks and fractures. After that, case studies using different types of elements are presented to demonstrate the effectiveness of the proposed methodology. The results using different types of elements are compared and discussed to illustrate the advantages of the EDFM.

2. Unstructured grids using the EbFVM

The EbFVM is a general approach that can be applied to both 2D and 3D unstructured grids. Because of its flexibility in the discretization of the domain and convenience of implementation in simulators that can construct arbitrary connections between gridblocks, this approach was implemented in UTCOMP-RS, an in-house, multi-component reservoir simulator for both two- and three-dimensional simulations (Marcondes and Sepehrnoori, 2010; Marcondes et al., 2013; Araújo et al., 2016; Fernandes et al., 2016). The simulator uses an implicit-pressure, explicit-composition (IMPEC) formulation. In each time step, the pressure equation is first implicitly solved, and then the component molar-balance equation is solved explicitly. In this section, the basic ideas of the EbFVM are introduced briefly. The types of elements, the subdivision of elements, and the evaluation of advective terms between matrix blocks are discussed.

3. Two-dimensional grids

For 2D simulations using the EbFVM, linear triangular and bi-linear quadrilateral elements can be used to construct the grids. The porosity and absolute permeability tensor are defined for each element, and other physical properties are evaluated at the vertices. Each element of the grid is divided into several sub-elements, and the conservation equations are integrated for each sub-element. For this reason, sub-elements are usually termed sub-control-volumes (SCVs). The conservation of mass is evaluated for the nodes of each element, giving rise to a cell-vertex approach. Herein, heterogeneous and anisotropic reservoirs can easily be handled with the EbFVM, as shown by Marcondes and Sepehrnoori (2010), Marcondes et al. (2013), and Santos et al. (2013), because all fluxes are evaluated on the interfaces of each SCV. In Fig. 1a, a 2D grid is shown. This grid contains thirteen vertices and nine elements. In Fig. 1b, each element in the grid is divided into several parts by connecting the centroid of the element to the middle points of the element edges. Therefore, each triangular element is divided into three parts, and each quadrilateral element is divided into four parts. Each part of the element is called an SCV. In the EbFVM, the control volume (CV) around each vertex of the grid is created through the contribution of all SCVs that share that vertex. In Fig. 1b, the CV around Vertex 4 (shown in red) is made up of SCVs from Elements 1, 4, 7, and 8. Using this approach, the total number of CVs is always the same as the number of vertices in the grid. Therefore, in Fig. 1b, a total number of thirteen CVs are created. In the simulator, physical properties such as pressure, phase saturation, and number of moles of each component are calculated for each CV. More details can be found in Marcondes and Sepehrnoori (2010) and Santos et al. (2013).

4. Three-dimensional grids

The basic concepts used in 3D grids are similar to those in 2D grids. However, 3D grids are typically much more complicated than 2D grids. Four types of elements can be used in 3D grids: tetrahedron, prism, hexahedron, and pyramid. Each element is discretized into several SCVs following a similar process as in 2D grids. Fig. 2 through 5 show the splitting of the tetrahedron, prism, hexahedron, and pyramid elements into SCVs, respectively. The splitting points are the middle points of element edges and the centroids of element faces. More details can be found in Marcondes et al. (2013).

After the discretization of the elements, the SCVs that share the same vertex will form a CV. Fig. 6a shows a 3D grid with three types of elements. These elements are split into SCVs, and the discretization is shown in Fig. 6b. In Fig. 6b, the SCVs that belong to one CV are shown in blue. It can be seen that each CV could have a very irregular geometry. Fig. 6c shows all CVs formed by SCVs.

5. Evaluation of flux

The reason elements are subdivided into SCVs in the EbFVM is to make it convenient to evaluate the flux between CVs. In this section, the approach to evaluating the flux in the EbFVM is discussed briefly.

As mentioned before, in the EbFVM, physical properties such as fluid pressure are evaluated at the vertices (or CVs). The coordinates and physical properties at any point inside an element can be approximated using the coordinates and properties at the vertices of the element. For 2D elements,

$$\begin{aligned} x(\xi,\eta) &= \sum_{i=1}^{N_v} N_i x_i; \\ y(\xi,\eta) &= \sum_{i=1}^{N_v} N_i y_i; \\ \Phi(\xi,\eta) &= \sum_{i=1}^{N_v} N_i \Phi_i. \end{aligned} \tag{1}$$

For 3D elements,

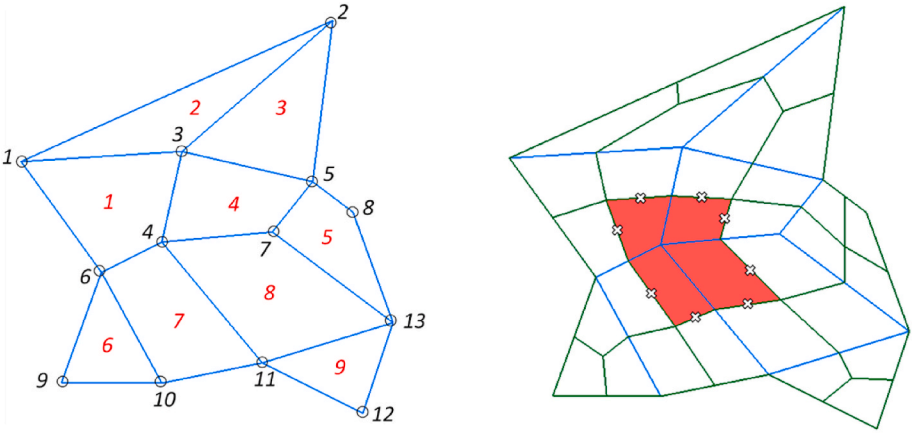

Fig. 1. Illustration of the elements and the creation of CVs in a 2D unstructured grid. (a) Elements. (b) Elements and CVs. The blue lines represent the boundaries of the elements, and the green lines represent the boundaries of the CVs. In (a), the thirteen vertices and nine elements are labeled in black and red, respectively. In (b), a CV containing four SCVs (around Vertex 4) is shown in red. The integration points for the CV are shown as well. (For interpretation of the references to color in this figure legend, the reader is referred to the Web version of this article.)

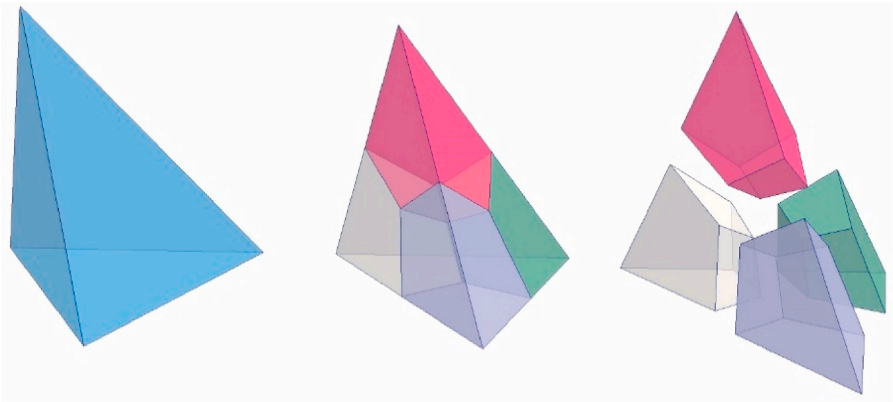

Fig. 2. Splitting of a tetrahedron element. The SCVs are shown in different colors. (For interpretation of the references to color in this figure legend, the reader is referred to the Web version of this article.)

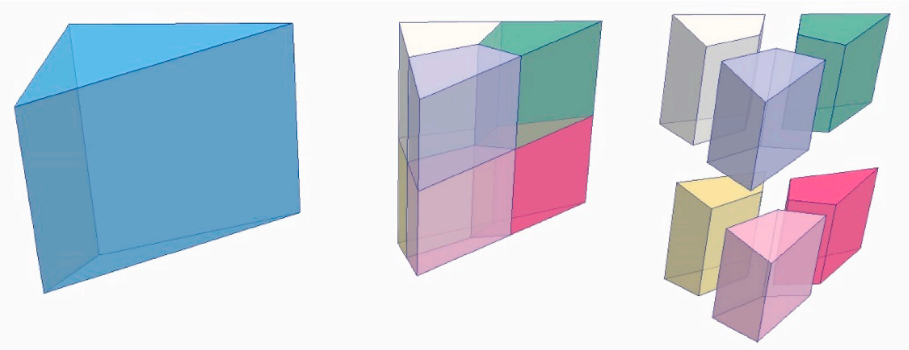

Fig. 3. Splitting of a prism element. The SCVs are shown in different colors. (For interpretation of the references to color in this figure legend, the reader is referred to the Web version of this article.)

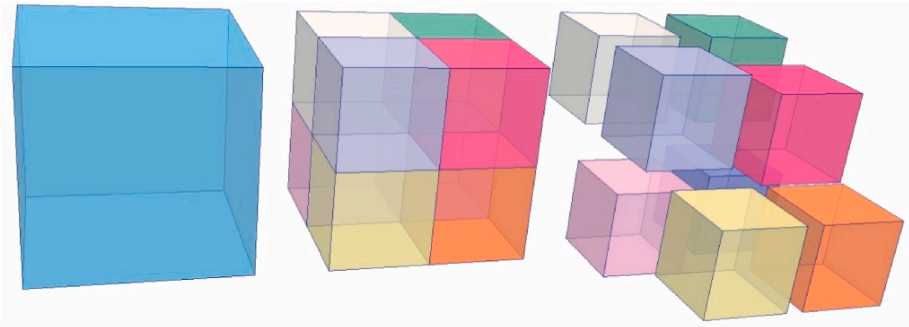

Fig. 4. Splitting of a hexahedron element. The SCVs are shown in different colors. (For interpretation of the references to color in this figure legend, the reader is referred to the Web version of this article.)

$$
\begin{aligned}
x(\xi,\eta,\gamma) &= \sum_{i=1}^{N_v} N_i x_i;\\
y(\xi,\eta,\gamma) &= \sum_{i=1}^{N_v} N_i y_i;\\
z(\xi,\eta,\gamma) &= \sum_{i=1}^{N_v} N_i z_i;\\
\Phi(\xi,\eta,\gamma) &= \sum_{i=1}^{N_v} N_i \Phi_i.
\end{aligned}
\tag{2}
$$

In Equations (1) and (2), x, y, and z are the Cartesian coordinates of a point in the element, ξ, η, and γ are the local coordinates of the point in the computational plane, Φ is the physical property value at the point, N_v is the number of vertices of the element, N_i is the *i-th* shape function, x_i, y_i, and z_i are the Cartesian coordinates of Vertex i, and Φ_i is the physical property value at Vertex i. The shape functions for 2D and 3D elements in the computational plane are presented in Appendix A.

Using Equations (1) and (2), the gradient of physical property Φ can be evaluated as

$$
\begin{aligned}
\frac{\partial \Phi}{\partial x} &= \sum_{i=1}^{N_v} \frac{\partial N_i}{\partial x}\Phi_i;\\
\frac{\partial \Phi}{\partial y} &= \sum_{i=1}^{N_v} \frac{\partial N_i}{\partial y}\Phi_i;\\
\frac{\partial \Phi}{\partial z} &= \sum_{i=1}^{N_v} \frac{\partial N_i}{\partial z}\Phi_i \quad \text{(for 3D elements)}.
\end{aligned}
\tag{3}
$$

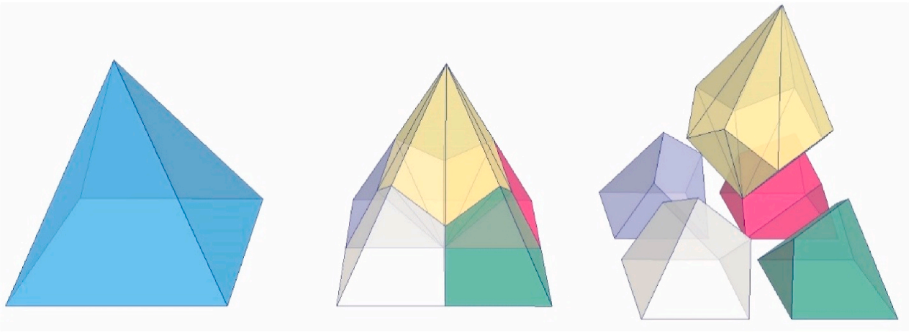

Fig. 5. Splitting of a pyramid element. The SCVs are shown in different colors. (For interpretation of the references to color in this figure legend, the reader is referred to the Web version of this article.)

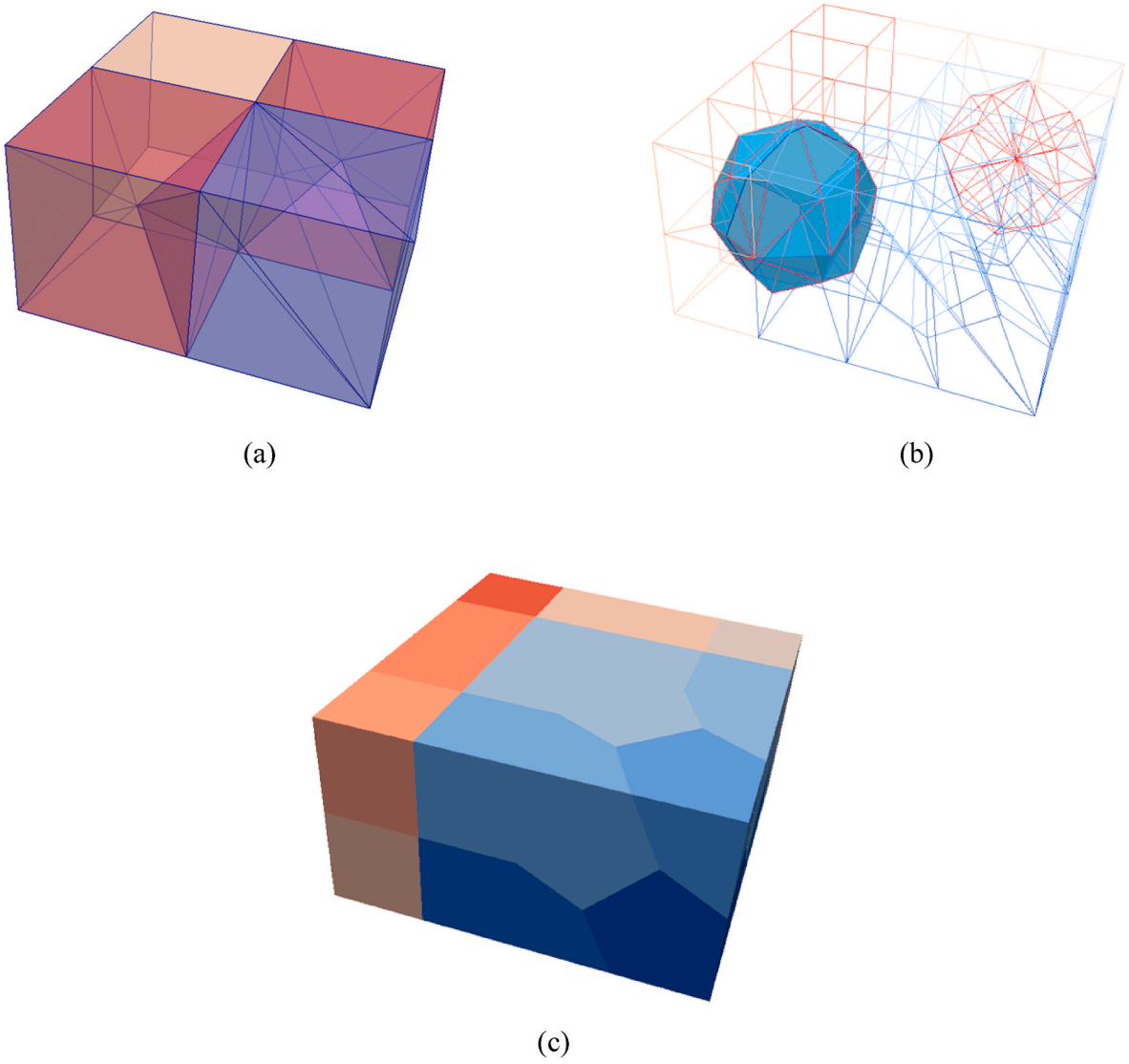

Fig. 6. Illustration of the construction of CVs in 3D grids. (a) A grid made up of ten tetrahedron elements (purple), one hexahedron element (orange), and ten pyramid elements (red). (b) Discretization of elements. A CV in the grid is shown in blue. (c) All CVs shown in different colors. (For interpretation of the references to color in this figure legend, the reader is referred to the Web version of this article.)

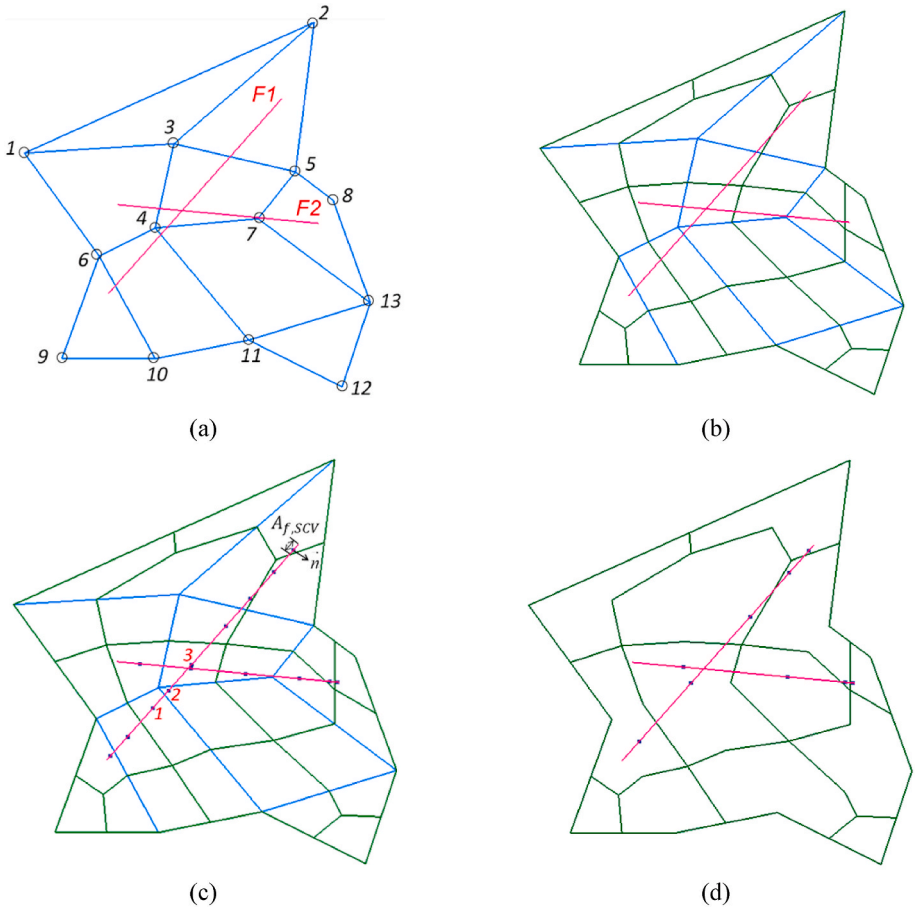

Fig. 7. Illustration of the procedure to obtain fracture segments and calculate matrix-fracture connections in 2D grids. The pink lines represent fractures ("F1" and "F2"), the blue lines represent the boundaries of elements, and the green lines represent the boundaries of control volumes. (a) Place fractures in the grid made up of elements. The vertices of the elements are labeled. (b) Split elements into SCVs. (c) Calculate intersections between fractures and SCVs. The center of each fracture segment is shown. (d) For each fracture, merge fracture segments within the same CV and calculate the connectivity factors between fracture segments and CVs. The center of each fracture segment after the merging process is shown. (For interpretation of the references to color in this figure legend, the reader is referred to the Web version of this article.)

For 2D grids, $\frac{\partial N_i}{\partial x}$ and $\frac{\partial N_i}{\partial y}$ can be obtained by solving the following linear system:

$$\begin{aligned}\frac{\partial N_i}{\partial \xi} &= \frac{\partial N_i}{\partial x}\frac{\partial x}{\partial \xi} + \frac{\partial N_i}{\partial y}\frac{\partial y}{\partial \xi};\\ \frac{\partial N_i}{\partial \eta} &= \frac{\partial N_i}{\partial x}\frac{\partial x}{\partial \eta} + \frac{\partial N_i}{\partial y}\frac{\partial y}{\partial \eta}.\end{aligned} \tag{4}$$

For 3D grids, the following system should be solved to obtain $\frac{\partial N_i}{\partial x}, \frac{\partial N_i}{\partial y}$, and $\frac{\partial N_i}{\partial z}$:

$$\begin{aligned}\frac{\partial N_i}{\partial \xi} &= \frac{\partial N_i}{\partial x}\frac{\partial x}{\partial \xi} + \frac{\partial N_i}{\partial y}\frac{\partial y}{\partial \xi} + \frac{\partial N_i}{\partial z}\frac{\partial z}{\partial \xi};\\ \frac{\partial N_i}{\partial \eta} &= \frac{\partial N_i}{\partial x}\frac{\partial x}{\partial \eta} + \frac{\partial N_i}{\partial y}\frac{\partial y}{\partial \eta} + \frac{\partial N_i}{\partial z}\frac{\partial z}{\partial \eta};\\ \frac{\partial N_i}{\partial \gamma} &= \frac{\partial N_i}{\partial x}\frac{\partial x}{\partial \gamma} + \frac{\partial N_i}{\partial y}\frac{\partial y}{\partial \gamma} + \frac{\partial N_i}{\partial z}\frac{\partial z}{\partial \gamma}.\end{aligned} \tag{5}$$

With the gradient of physical properties, e.g., flow potential gradient, the total molar flow rate of component k across the boundaries of an SCV through advection can be evaluated through

$$F_k = \sum_{l=1}^{n_{ip}} \sum_{j=1}^{n_p} x_{kj}\xi_j \frac{k_{rj}}{\mu_j} \overrightarrow{\overrightarrow{K}} \cdot \overrightarrow{\nabla}\Phi_{jl}\overrightarrow{A_l}, \tag{6}$$

where n_{ip} is the number of integration points associated with the SCV, n_p is the number of phases, x_{kj} is the mole fraction of component k in phase j, ξ_j is the molar density of phase j, k_{rj} is the relative permeability of phase j, μ_j is the viscosity of phase j, $\overrightarrow{\overrightarrow{K}}$ is the permeability tensor, $\overrightarrow{\nabla}\Phi_{jl}$ is the flow potential gradient in phase j at the l^{th} integration point evaluated by Equation (3), and $\overrightarrow{A_l}$ is the area of the interface. Here, each integration point is the center of the interface between two SCVs. It should be noted that the integration is performed on every interface between two SCVs within the same element. The integration points in 2D elements are shown in Appendix A, Figure A.1. There are three and four integration points in each triangular and quadrilateral element, respectively. For 3D elements, the interfaces can also be easily found in Fig. 2 through 5 (between each pair of SCVs). The number of integration points in each tetrahedron, prism, hexahedron, and pyramid element is 6, 9, 12, and 8, respectively. Because the integration is always calculated within the element, the same permeability value can be used on both sides of the interface, and no interpolation is required for the evaluation of flux. The fluid properties in Equation (6) are evaluated by an upstream scheme depending on the sign of $\overrightarrow{\overrightarrow{K}}\cdot\overrightarrow{\nabla}\Phi_{jl}\overrightarrow{A_l}$.

Ignoring the physical dispersion term, the material balance equation used in the simulator is

$$\frac{\partial N_k}{\partial t} = F_k + q_k, \quad k = 1, \ldots, n_c + 1 \tag{7}$$

where N_k is the number of moles of component k, q_k is the injection/production molar rate of component k from wells, and n_c is the number of hydrocarbon components. Component $n_c + 1$ denotes the water component. In the EbFVM, Equation (7) is integrated for every SCV of every element. After that, an assembly process is performed using all SCVs that share the same vertex (within the same CV). Overall, the calculations are performed within each element, and the assembly process is performed to obtain the material balance equation for each CV.

It should also be noted that wells are defined at vertices in the EbFVM. For a well with a constant rate, the well flow rate can be directly applied in the material balance equation of the corresponding CV. For a well with constant bottomhole pressure, the well index can be calculated by finding an equivalent radius of the CV that contains the well. See Fung et al. (1992) for more details in the derivation. A radial flow around the well is assumed in their derivation.

6. Basic EDFM methodology

The basic idea of the EDFM combines the dual-continuum concept with discrete fracture modeling. Different from most DFMs, the EDFM uses non-conforming meshes. In this approach, the first step is to perform the matrix gridding without taking into account the fracture locations. Subsequently, the fractures are placed inside the reservoir, and they are discretized by matrix block boundaries. Each small piece of the fracture in a matrix block is referred to as a "fracture segment". With such discretization, each fracture segment is physically connected to only one matrix block. These fracture segments are represented by CVs (referred to as "fracture CVs") in a separate domain from the matrix. To allow fluid flow within the fracture domain and between the matrix and the fracture domain, special connections are constructed. In summary, three types of connections are considered in the EDFM (Moinfar et al., 2014; Xu et al., 2017):

Type I: matrix-fracture connection between a matrix block and the fracture segment inside it.

Type II: fracture-fracture connection between two fracture segments belonging to the same fracture. This type of connection allows for flow within a fracture.

Type III: fracture-fracture connection between two fracture segments that intersect each other. This type of connection allows for fluid flow within fracture networks.

In reservoir simulators, the above-mentioned three types of connections are typically represented by non-neighboring connections (NNCs).

The EDFM also considers the flow between fractures and wellbores, which is typically seen for fractured wells. In such cases, the fracture CVs are treated as regular blocks, and effective well-indices are calculated and assigned to the corresponding fracture segments that intersect the well trajectories. More details on the calculation of effective well-indices can be found in Moinfar et al. (2013) and Xu and Sepehrnoori (2019).

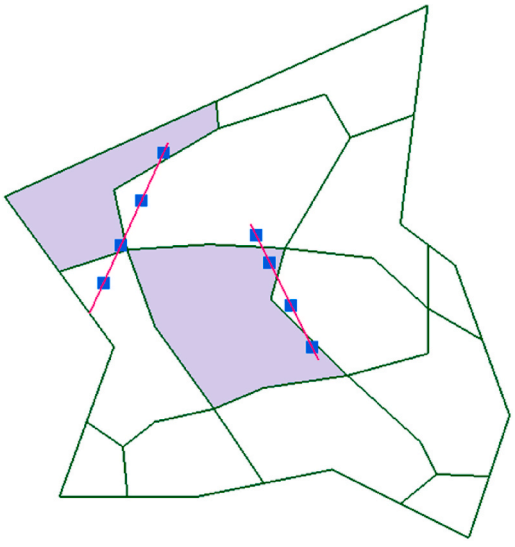

Fig. 8. A 2D example where the fracture segments in a CV are merged into multiple fracture segments. The green lines are the boundaries of CVs. The blue dots represent the center of each fracture segments. The two CVs shown in purple contain multiple fracture segments from a single fracture. (For interpretation of the references to color in this figure legend, the reader is referred to the Web version of this article.)

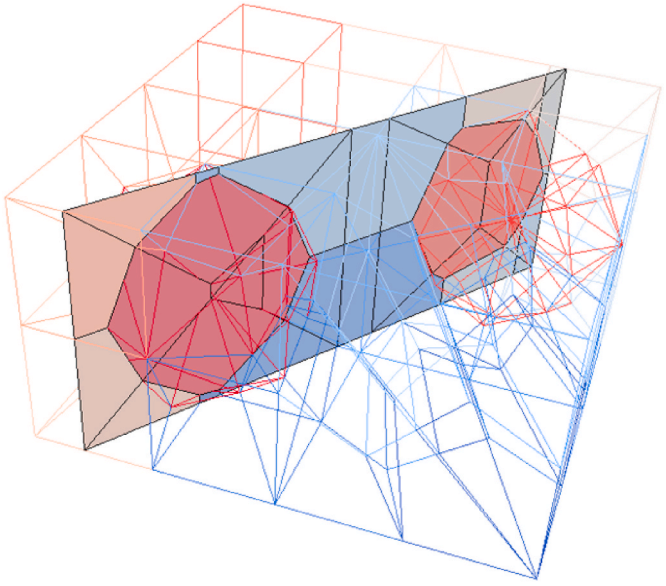

Fig. 9. Illustration of the calculation of matrix-fracture connections in a 3D grid. The fracture segments (before merging) that are contained in the same CV are shown in the same color. (For interpretation of the references to color in this figure legend, the reader is referred to the Web version of this article.)

7. EDFM in unstructured grids using the EbFVM

The concept used to apply the EDFM to unstructured grids is similar to that used in Cartesian and corner-point grids. Additional CVs need to be created in the computational domain to represent the fracture segments, and NNCs need to be constructed inside the simulator to represent different types of flow between fractures and matrix gridblocks crossed by fractures. The main challenges are in the discretization of fractures and the calculation of transmissibility factors for matrix-fracture connections. In the EbFVM, the matrix permeability is defined on elements. However, the solution variables (e.g., pressure, saturation) are defined on vertices (or CVs). On the basis of these unique features, a methodology is proposed here to conduct the geometrical calculations of matrix-fracture intersections on SCVs.

Fig. 7 illustrates the procedure to obtain fracture segments and calculate matrix-fracture connections. Initially, the fractures are placed inside the grid which is made up of elements (Fig. 7a). The elements are then divided into SCVs for geometrical calculation (Fig. 7b). The intersections between the fracture polygons and SCVs are calculated. During the calculation, each SCV is treated as a general polyhedron. It should be noted that the geometrical calculations of fracture-SCV intersections are not trivial. The geometrical algorithm developed by Xu and Sepehrnoori (2019) for corner-point grids is applied here. After the calculation, the fractures are discretized into a series of fracture segments, and each fracture segment is contained in an SCV, as shown in Fig. 7c. The transmissibility factor between an SCV and a fracture segment inside it can be evaluated in a similar manner as in Xu et al. (2017):

$$T_{f-SCV} = \frac{2A_{f,SCV}\,\vec{n}\cdot\left(\vec{\vec{K}}_{SCV}\cdot\vec{n}\right)}{d_{f-CV}}, \tag{8}$$

where $A_{f,SCV}$ is the area of the fracture segment in the SCV, $\vec{n}$ is the unit normal vector of the fracture plane, $\vec{\vec{K}}_{SCV}$ is the permeability tensor of the SCV, which is the same as the permeability tensor of the corresponding element, and d_{f-CV} is the average normal distance from the fracture segment to the CV that the SCV belongs to. For illustration purposes, in Fig. 7c, $A_{f,SCV}$ and $\vec{n}$ for a fracture segment is shown. The derivation of Equation (8) (Xu et al., 2017) assumes a "linear pressure distribution" in the CV, which is suitable for cases where all SCVs in the CV have the same porosity and permeability. For reservoirs with heterogeneous porosity and permeability fields, which leads to piecewise linear pressure distribution within the CV, Equation (8) is a rough approximation, and more studies are needed on the calculation of matrix-fracture transmissibility factors.

In the last step, the fracture segments belonging to the same fracture and contained in the same CV are merged if they share a common edge, and the corresponding fracture-SCV transmissibility factors are added together. As an example, in Fig. 7c, the three fracture segments ("1," "2," and "3") belonging to Fracture "F1" in the CV around Vertex 4 are merged into one fracture segment, as shown in Fig. 7d. The purpose of merging the fracture segments is to reduce the number of fracture segments (equaling the number of CVs) for each fracture. After the merging process, the transmissibility factor between a CV and the fracture segment inside it is calculated as

$$T_{f-CV} = \sum_{i=1}^{n_{merge}} T_{f-SCV,i}, \tag{9}$$

where n_{merge} is the number of initial fracture segments that are merged (in Fig. 7c).

For 2D grids, it should be noted that because some CVs have a concave geometry, not all fracture segments in a CV can be merged into one. It is possible for a fracture to have multiple fracture segments in a single CV. Fig. 8 presents an example of this situation.

For 3D grids, similarly, it is not always the case that all fracture segments in a CV that belong to the same fracture can be merged into

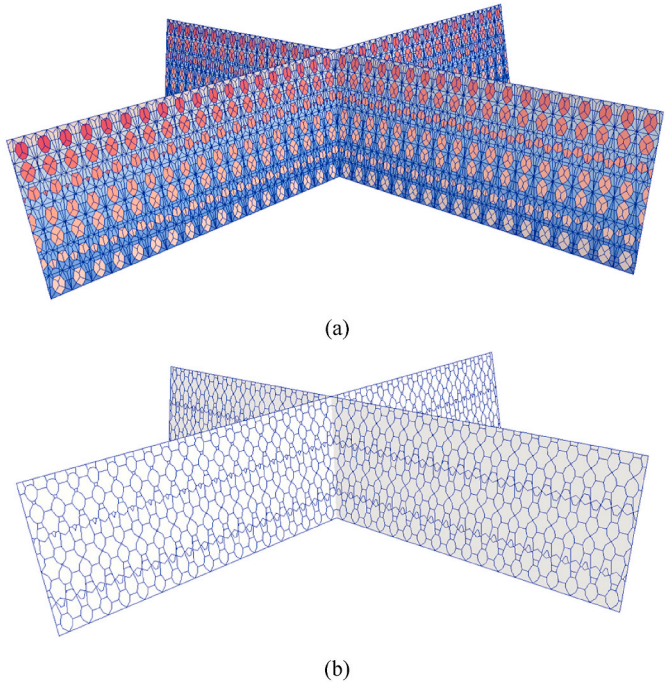

Fig. 10. Illustration of fracture segment merging in a 3D example where two fractures are placed in a grid made up of pyramid elements. (a) The fracture segments before the merging process. The fracture segments that are contained in the same CV are shown in the same color. (b) The fracture segments after the merging process. (For interpretation of the references to color in this figure legend, the reader is referred to the Web version of this article.)

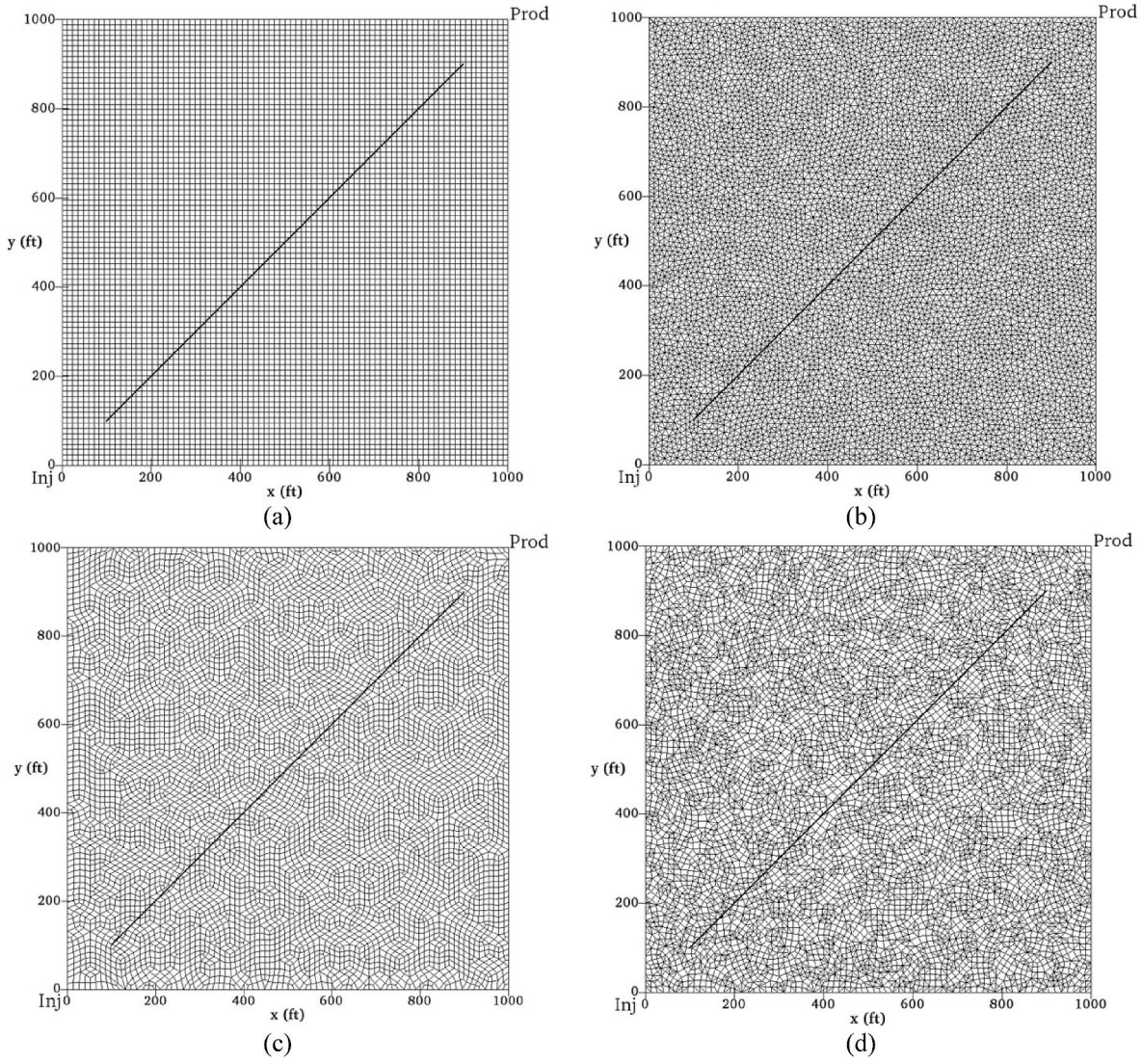

Fig. 11. Four different simulation grids and the locations of wells and the fracture in Case 1. The water injector ("Inj") is located at (0, 0), and the producer ("Prod") is located at (1000, 1000). The black line represents the fracture. For the matrix grids, the elements are shown. (a) 7056 square elements (7225 vertices). (b) 13650 triangular elements (6970 vertices). (c) 6868 quadrilateral elements (7021 vertices). (d) 9904 mixed triangular and quadrilateral elements (7053 vertices).

Table 1
Summary of key simulation parameters in Case 1.

Parameter	Value	Unit	Parameter	Value	Unit
Reservoir permeability	200	md	Residual water saturation	0.24	–
Reservoir porosity	0.25	–	Residual oil saturation	0.2	–
Initial reservoir pressure	4500	psi	Water rel. perm. endpoint	0.4	–
Reservoir thickness	50	ft	Oil rel. perm. endpoint	0.6	–
Rock compressibility	3×10^{-6}	psi^{-1}	Water rel. perm. exponent	2.0	–
Reservoir temperature	200	°F	Oil rel. perm. exponent	3.0	–
Water viscosity	0.3	cp	Water injection rate	700	STB/day
Initial water saturation	0.3	–	Producer bottomhole pressure	4000	psi
Wellbore radius	0.5	ft			

one fracture segment. In addition, the merging of fracture segments is more complicated compared with that in 2D cases. Fig. 9 presents an example where a fracture is placed in the grid shown in Fig. 6. The fracture segments contained in the same CV are shown in the same color, and these fracture segments are to be merged. Fig. 10 presents a larger example of the merging of fracture segments. In Fig. 10, the number of fracture segments decreases from 12348 to 1823 through the merging process. It should be noted that because on average each CV contains more SCVs in 3D grids compared with that in 2D grids, the fracture segment merging step is more beneficial in reducing the number of fracture CVs in 3D grids.

The transmissibility factor calculations for other types of NNCs and well-fracture intersections in the EDFM are very similar to those in Cartesian and corner-point grids (Moinfar et al., 2014; Xu et al., 2017; and Xu and Sepehrnoori, 2019). All the newly calculated connections are sent to the simulator, which is similar to the case of structured grids.

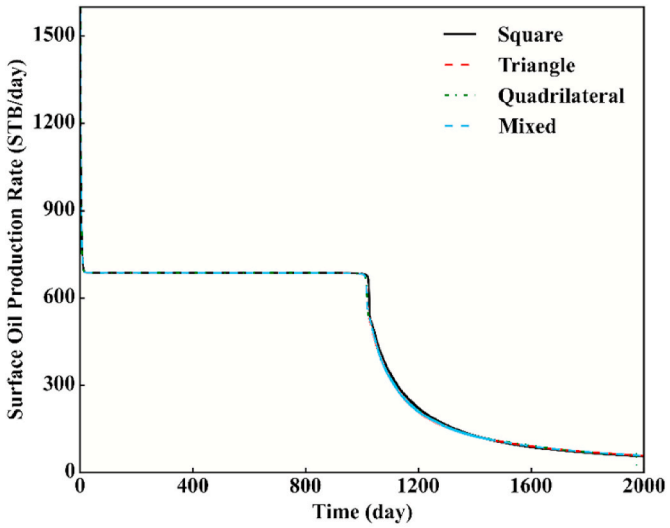

(a)

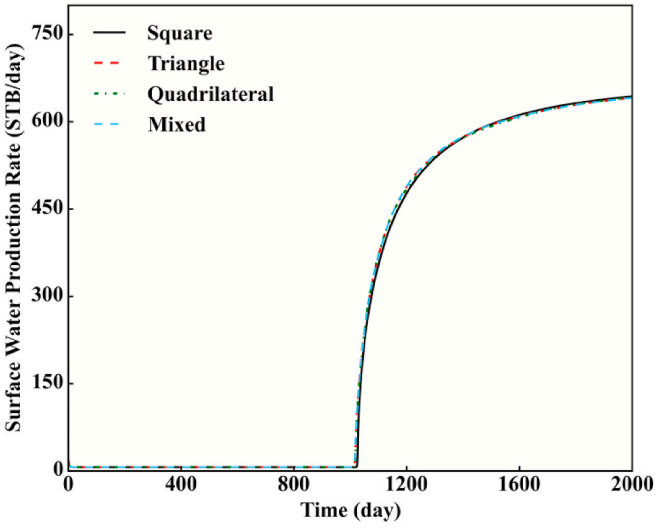

(b)

Fig. 12. Comparison of surface oil and water production rate without fracture. (a) Oil production rate. (b) Water production rate. "Square", "Triangle", "Quadrilateral", and "Mixed" represent the results using the simulation grids shown in Fig. 11a through 11d, respectively.

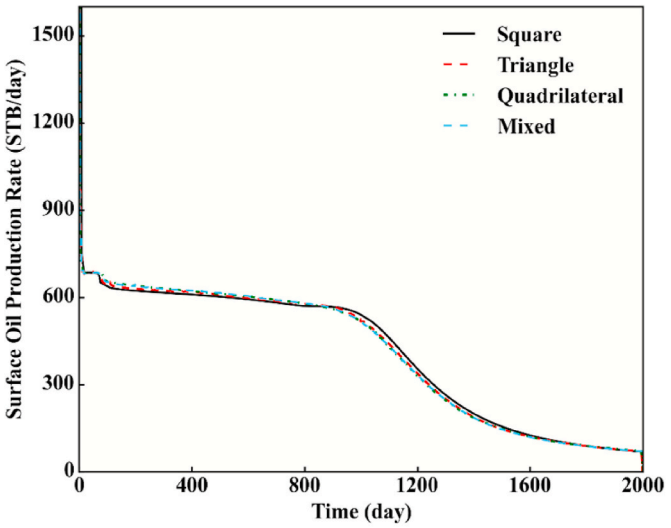

(a)

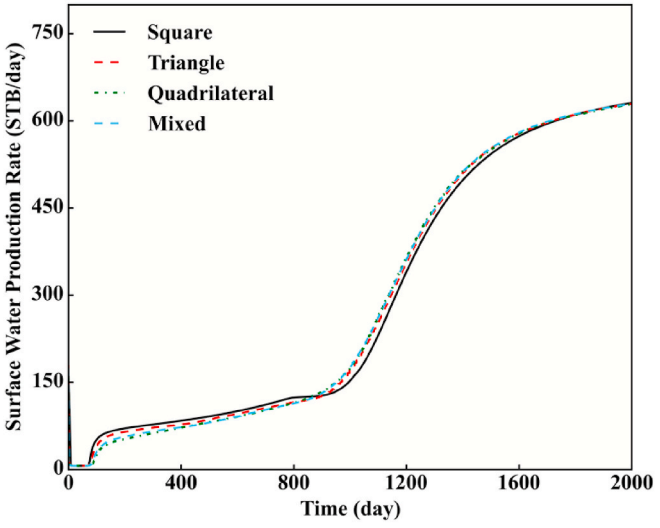

(b)

Fig. 13. Comparison of surface oil and water production rate for simulations with the fracture. "Square", "Triangle", "Quadrilateral", and "Mixed" represent the results using the simulation grids shown in Fig. 11a through 11d, respectively.

8. Case studies for two-dimensional unstructured grids using the EbFVM

The methodology discussed in the previous section was implemented in an EDFM preprocessing code. In this section and the following sections, case studies are presented using both 2D and 3D grids. As a way of showing the generality of the implementation, all types of 2D and 3D elements are used in the simulations. Cases 1, 2, and 3 are simulations of secondary recovery processes with natural fractures, and Cases 4 and 5 are simulations of primary recovery in hydraulically fractured reservoirs. The results of the case studies show the convenience and effectiveness of using the proposed methodology to simulate arbitrarily oriented fractures.

8.1. Case 1: Homogeneous reservoir with different matrix gridding

In this case study, a waterflooding process in a homogeneous reservoir with a long natural fracture is simulated. The reservoir dimensions are $1000 \times 1000 \times 50$ ft. Four different simulation grids with a similar number of vertices (or CVs) are used for result comparison, as shown in Fig. 11. The first grid has only square elements, making it like a regular Cartesian grid; the second grid is made up of triangular elements; the third grid has only quadrilateral elements; the last grid is a mixture of triangular and quadrilateral elements. A long fracture is placed inside the reservoir, as shown in Fig. 11. The fracture width is 0.01 ft, and the fracture permeability is 3×10^6 md. A water injector with a constant injection rate and an oil producer with a constant bottomhole pressure

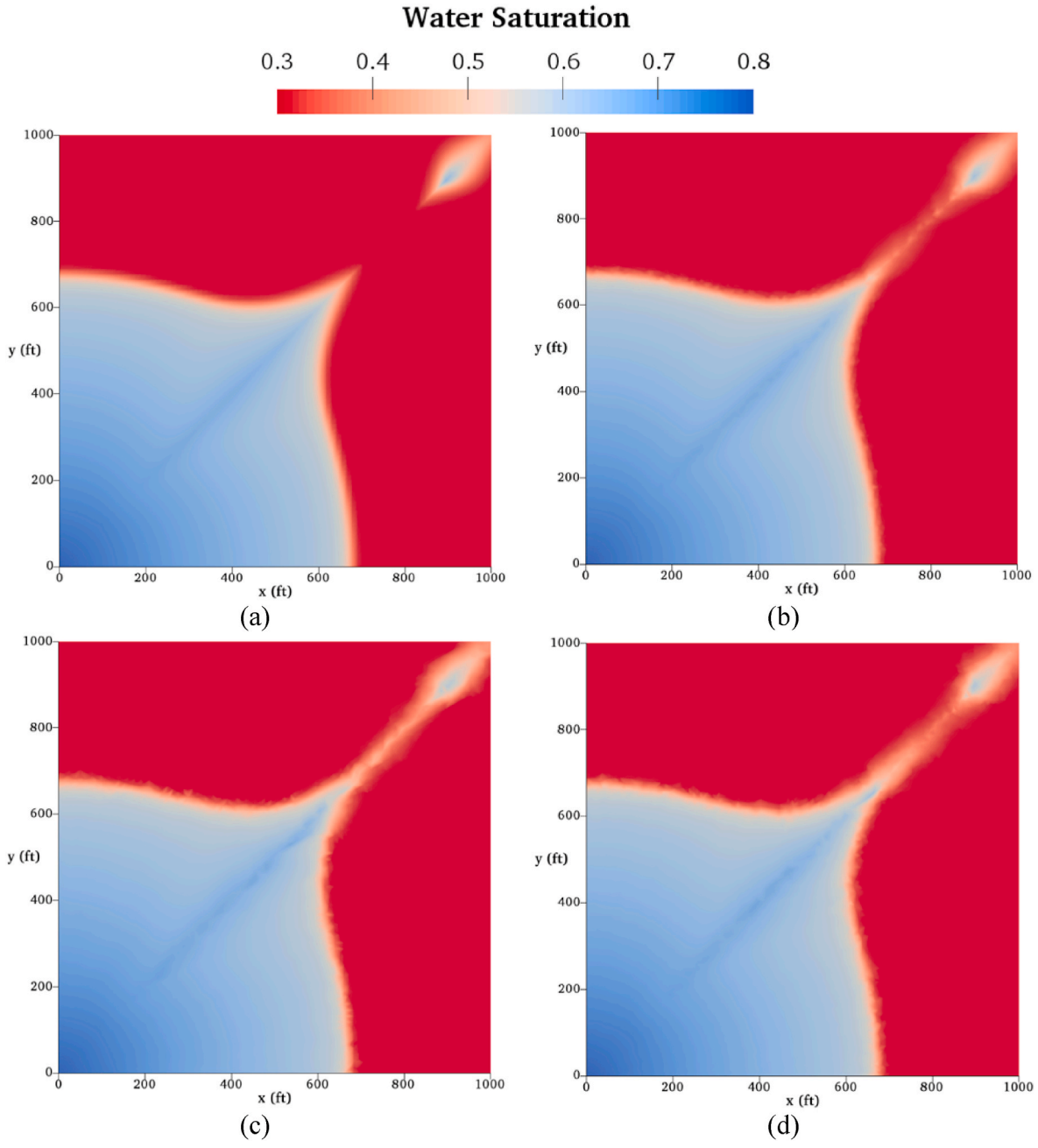

Fig. 14. Water saturation profiles at 500 days. (a)–(d) Results obtained from the simulation grids shown in Fig. 11a through 11d, respectively.

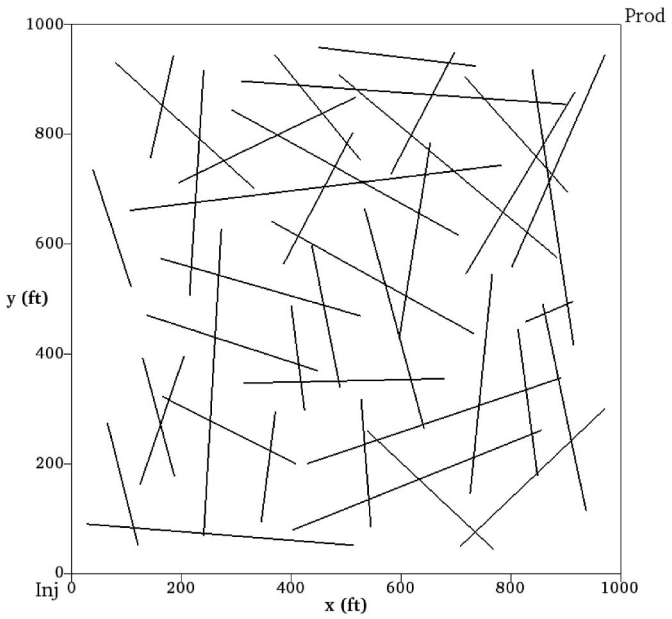

Fig. 15. Locations of wells and the 41 fractures in Case 2. The injector ("Inj") is located at (0, 0), and the producer ("Prod") is located at (1000, 1000). The black lines represent fractures.

are placed at two corners of the reservoir, as shown in Fig. 11. Table 1 summarizes the basic parameters for the simulation. In this case study, the oil phase is composed of only one hydrocarbon component (C_{20}), and a two-phase (water and oil) flow is simulated. Corey-type relative permeability curves are used, and the parameters of the relative permeability curves are also provided in Table 1. The capillary effect is not considered in this study.

Fig. 12 presents the simulated oil and water flow rate on the four different grids without considering the fracture. It can be seen that similar results were obtained using all four grids, indicating that the EbFVM formulation provides reliable results on all the grids shown in Fig. 11.

Fig. 13 presents the predicted oil and water flow rate for simulations that consider the impact of the fracture. Fig. 14 shows the water saturation profiles at 500 days, where the impact of the long fracture can be clearly observed. Due to the grid orientation effect and the influence of numerical dispersion, a difference in water saturation distribution in some regions can be observed. Overall, similar results were obtained for the oil and water flow rate and the water saturation from all four grids, which verifies the effectiveness of the proposed methodology to apply the EDFM to 2D unstructured grids.

8.2. *Case 2: Homogeneous reservoir with 41 natural fractures*

A primary advantage of the EDFM is that fractures with arbitrary orientations can be conveniently simulated. Here, the four simulation grids in Case 1 are used, but more fractures with different orientations are placed in the reservoir, as shown in Fig. 15. As can be seen, the fractures form a fracture network. The reservoir and fracture properties are the same as in Case 1.

Fig. 16 compares the oil and water rate curves obtained from the simulations on all four grids. Fig. 17 presents the water saturation profiles in the matrix at 500 days. The results obtained with the four

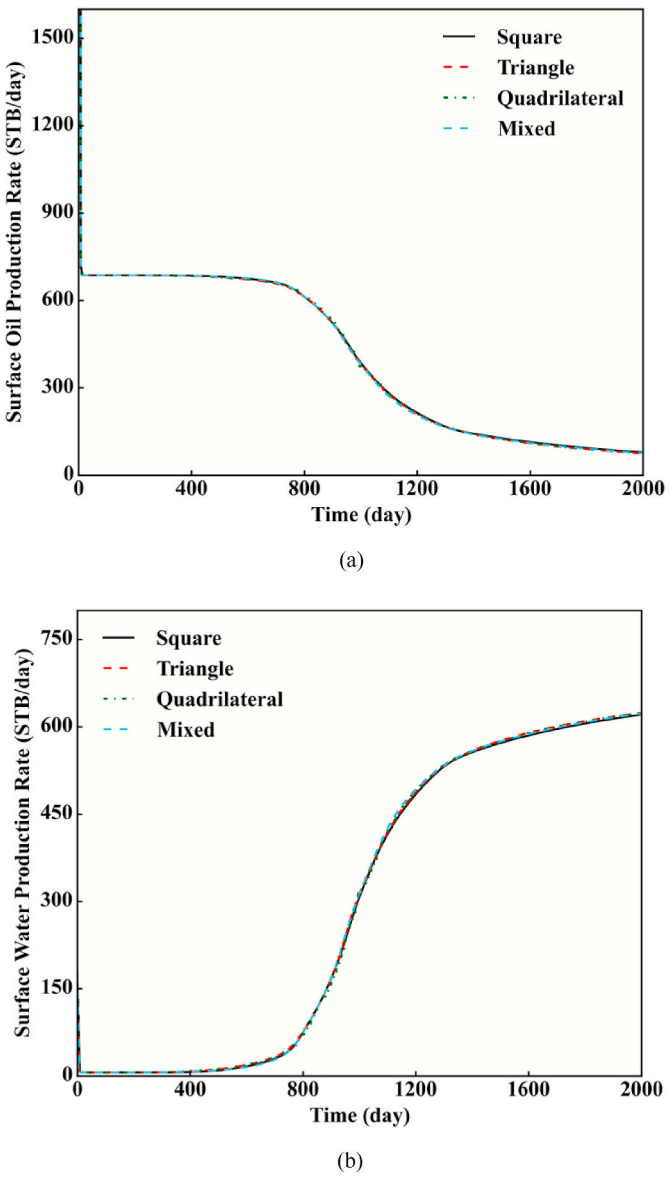

Fig. 16. Comparison of surface oil and water production rate for the case with 41 fractures using the four simulation grids in Fig. 11. (a) Oil production rate. (b) Water production rate. "Square", "Triangle", "Quadrilateral", and "Mixed" represent the results using the simulation grids shown in Fig. 11a through 11d, respectively.

different grids are very similar, showing the effectiveness of the methodology for simulating complex fracture networks with arbitrary fracture orientations. The physical properties in the fracture network were also calculated during the simulation. Fig. 18 shows the predicted water saturation in the fracture network at 500 days using the matrix grid in Fig. 11d.

Using the results obtained from the grid in Fig. 11a as a reference solution, we also calculate the L_2-error of water saturation on the other grids in Fig. 11 to quantify the difference between the simulation results using different grids. The L_2-error of water saturation over the entire domain is calculated as

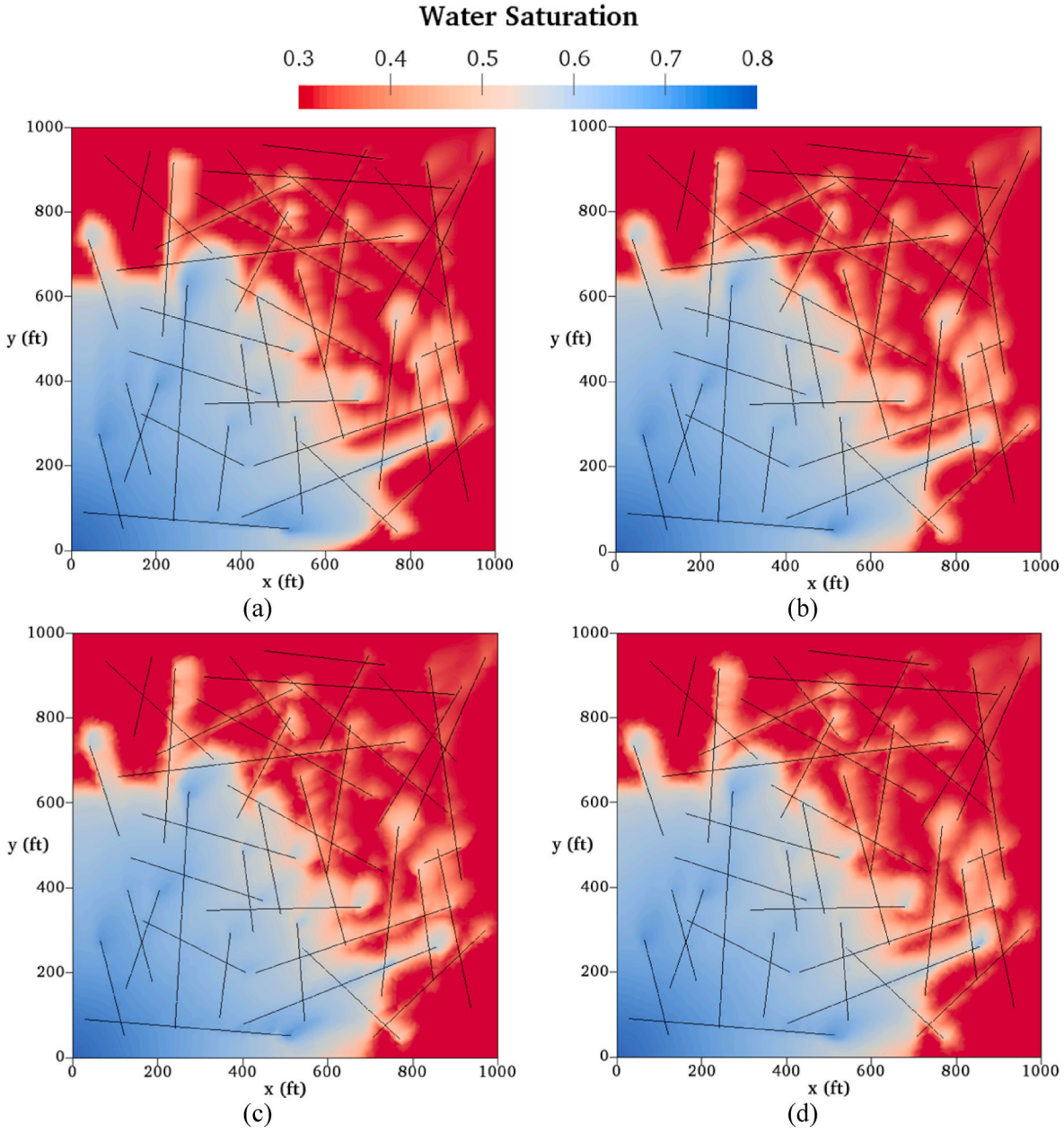

Fig. 17. Predicted water saturation profiles in the matrix at 500 days. (a)–(d) Results obtained with the simulation grids shown in Fig. 11a through 11d, respectively. The locations of fractures are also shown.

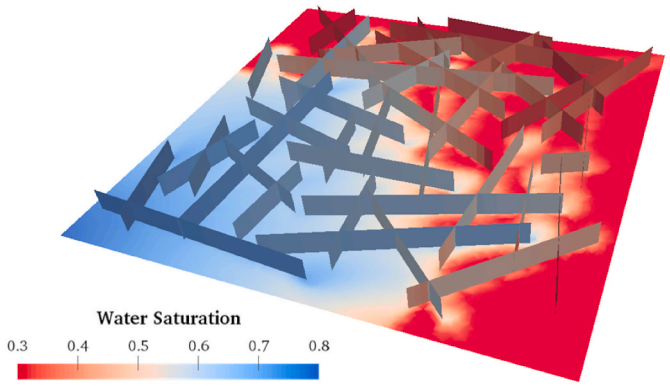

Fig. 18. Predicted water saturation in the fracture network at 500 days using the matrix grid shown in Fig. 11d. The water saturation in the matrix is also shown.

Table 2
Water saturation L_2-errors at 500 days in Cases 1 and 2. The results obtained from the grid in Fig. 11a are used as the reference solution.

	Triangular elements (Fig. 11b)	Quadrilateral elements (Fig. 11c)	Mixed elements (Fig. 11d)
Case 1, no fracture	0.0045	0.0048	0.0053
Case 1, one fracture	0.0072	0.0138	0.0140
Case 2, 41 fractures	0.0177	0.0174	0.0182

$$Err_{L_2} = \sqrt{\frac{1}{n_v}\sum_{i=1}^{n_v}\left(S_{w,i} - S_{w,i,ref}\right)^2}, \tag{10}$$

where n_v is the total number of vertices in the reference grid, $S_{w,i}$ is the interpolated water saturation at the location of the *i-th* vertex, and $S_{w,i,ref}$ is the water saturation at the *i-th* vertex in the reference solution. Table 2 reported the L_2-errors of water saturation in both Cases 1 and 2. It can be seen that as the complexity of fracture network increases, the L_2-error of water saturation also increases. Fig. 19 presents the water saturation difference profiles for Case 2. The difference is mainly in the near-fracture regions, partly due to the fact that the simulated water saturation distribution in these regions is largely affected by the local matrix gridding. Local refinement could be used to improve the simulation results in these regions, as reported by Panfili et al. (2015) and Yang et al. (2018). In other regions, the results have a good match. Overall, the difference between the results using different grids is relatively low.

Comparing Cases 1 and 2, it can be seen that the same matrix grids could be used to simulate different fractures. This is a unique advantage of using non-conforming meshes. With the EDFM, minimum adjustment of the original matrix grid is required, which provides a highly convenient approach to performing history matching and sensitivity studies with different realizations of fracture geometries.

8.3. Case 3: Reservoir with irregular geometry

In this case study, a 2D reservoir model with irregular geometry is used, as shown in Fig. 20. This reservoir is represented by an unstructured grid with mixed elements. The total number of vertices is 11857, and the total number of elements is 13080. The reservoir thickness is 100 ft. A water injector ("Inj") and two producers ("Prod1" and "Prod2") are placed inside the reservoir. The injector has a constant injection rate, and the producers have a constant well bottomhole pressure. Twelve long fractures are placed in the reservoir. The fracture width and fracture permeability are 0.01 ft and 1.0×10^6 md, respectively. Other key simulation parameters are summarized in Table 3. In this compositional simulation, three non-water components are considered. Their original composition and properties are summarized in Table 4. A Corey-type relative permeability model is used, and the parameters of the relative permeability curves are presented in Table 5. The capillary pressure effect is not considered here.

Fig. 21 presents the predicted water, oil, and gas production rate curves. The water breakthrough occurs at approximately 1000 days, with a sharp increase in water production rate and a decrease in oil and gas production rates. Fig. 22 shows the water saturation profiles in the matrix at 500 and 1000 days, where the movement of water through the fracture network can be clearly observed. The influence of the reservoir geometry can also be seen, as the injected water moves along the irregular reservoir boundary.

9. Case studies for three-dimensional unstructured grids using the EbFVM

9.1. Case 4: Tight gas reservoir with inclined hydraulic fractures

This study focuses on primary production from a hydraulically fractured horizontal well in a tight gas reservoir. The reservoir dimensions are $2000 \times 1600 \times 100$ ft. A horizontal well and four inclined hydraulic fractures are placed at the center of the reservoir, as shown in Fig. 23. The dip of the fractures is 70°, and the fracture width and fracture permeability are 0.01 ft and 10000 md, respectively. All fractures fully penetrate the reservoir in the vertical direction. For verifying the implementation of the EDFM in grids with different types of elements, four matrix grids are created. The numbers of vertices and elements in the four grids are summarized in Table 6. As can be seen, all four grids have a similar number of vertices (or CVs), but they are made up of different types of elements. The grid with mixed elements (Grid D in Table 6) is shown in Fig. 24. Initially, water is at irreducible saturation, and the hydrocarbon component is methane. The other key simulation parameters are summarized in Table 7.

Fig. 25 compares the predicted gas production rates using the four grids. Fig. 26 presents the pressure profiles in the matrix after 1000 days of production. As can be observed, an excellent match was obtained between the results using different grids. This verifies the methodology to apply the EDFM to 3D unstructured grids with different types of elements. Together with the results of Cases 1 and 2, it shows the high flexibility of the EDFM. Different grids with different types of elements (2D or 3D) could be conveniently used in conjunction with the EDFM to simulate fractured reservoirs. The accuracy of the long-term prediction using the EDFM is not significantly affected by the type of elements used in the grid.

9.2. Case 5: 3D reservoir with complex geometry

In this case, a 3D reservoir model with irregular geometry is used for the simulation, as shown in Fig. 27. The reservoir is represented by an unstructured grid with 42232 vertices and 44115 elements, including 4200 tetrahedron elements, 35715 hexahedron elements, and 4200

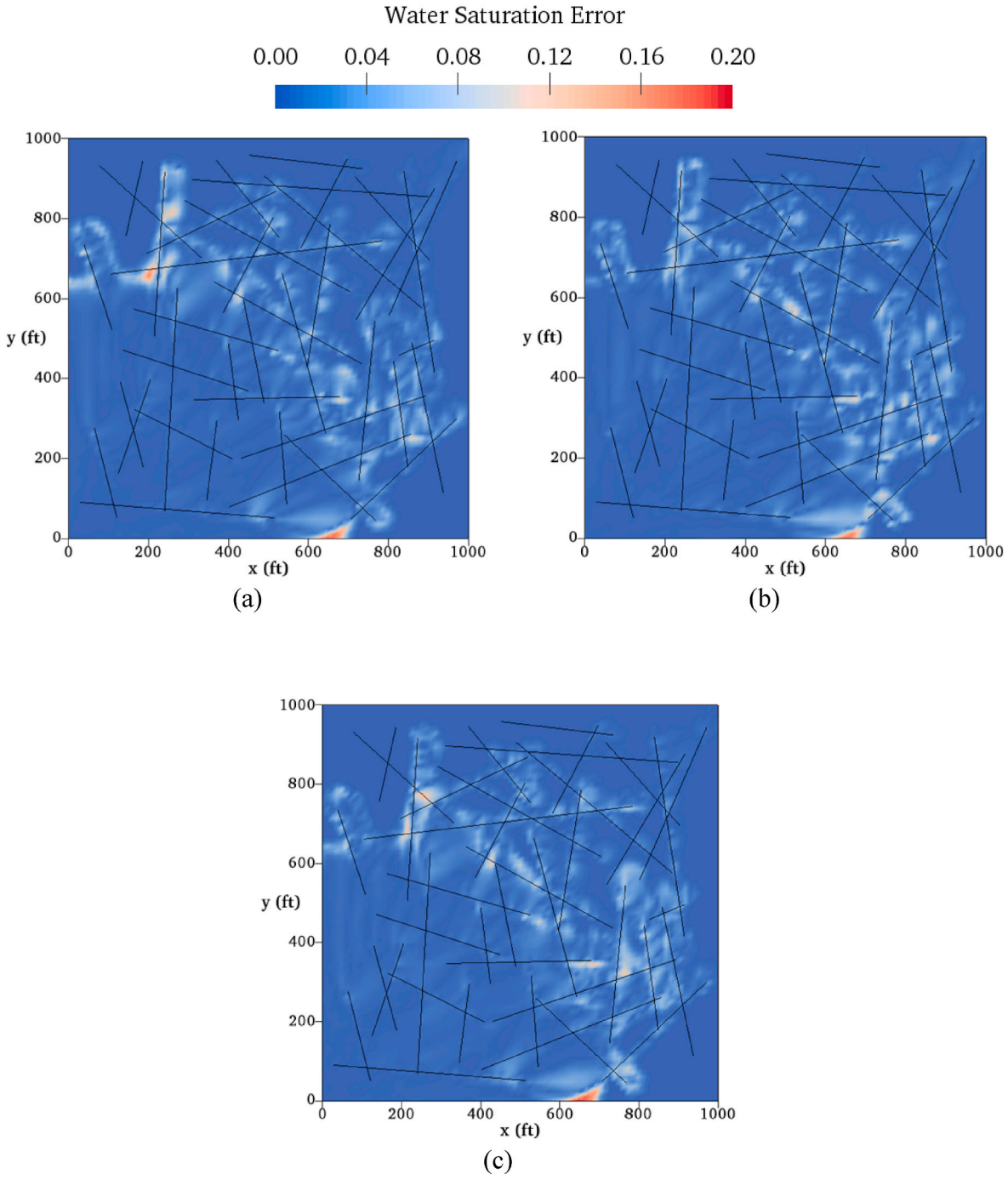

Fig. 19. Matrix water saturation difference profiles at 500 days for the cases with 41 fractures. (a)–(c) Difference between the results obtained from the simulation grids in Fig. 11b through 11d and the result obtained from the grid in Fig. 11a, respectively. The locations of fractures are also shown.

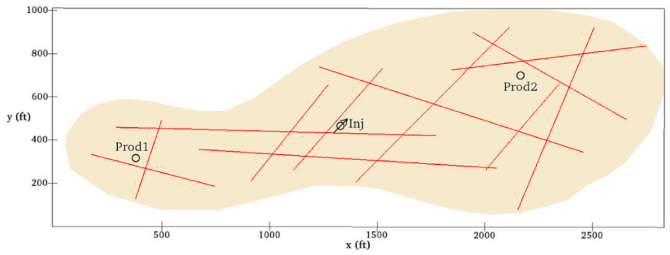

Fig. 20. Reservoir geometry, locations of fractures (shown as red lines), and locations of wells in Case 3. "Inj" is water injector and "Prod1" and "Prod2" are producers. (For interpretation of the references to color in this figure legend, the reader is referred to the Web version of this article.)

Table 3
Summary of key simulation parameters in Case 3.

Parameter	Value	Unit	Parameter	Value	Unit
Reservoir permeability	200	md	Initial water saturation	0.3	–
Reservoir porosity	0.3	–	Water compressibility	1×10^{-6}	psi^{-1}
Initial reservoir pressure	2000	psi	Well bottomhole pressure	1500	psi
Reservoir temperature	160	°F	Gas injection rate	3000	STB/day
Rock compressibility	3×10^{-6}	psi^{-1}	Wellbore radius	0.5	ft
Water viscosity	0.8	cp			

Table 4
Properties of hydrocarbon components in Case 3.

Component	CO_2	CH_4	NC16
Molar fraction	0.01	0.19	0.80
Molecular weight (lb/lb-mol)	44.0	16.0	222.0
Critical pressure (psi)	1071.6	667.2	252.1
Critical volume (ft^3/lb-mol)	1.505	1.586	13.087
Critical temperature (K)	304.2	190.6	734.7
Acentric factor	0.225	0.008	0.684
Parachor	49.0	77.0	831.9

Table 5
Parameters of water, oil, and gas relative permeability curves in Case 3.

Parameter	Value	Parameter	Value
Residual water saturation	0.2	Gas rel. perm. endpoint	0.9
Residual oil saturation	0.1	Water rel. perm. exponent	3.0
Residual gas saturation	0	Oil rel. perm. exponent	2.0
Water rel. perm. endpoint	0.4	Gas rel. perm. exponent	2.0
Oil rel. perm. endpoint	0.9		

pyramid elements. This grid was used by Araújo et al. (2016) for a gas-flooding simulation. As can be seen, a "hole" was added in this grid to represent a low-permeability zone. Unlike the case of structured grids, no non-active cells need to be used for the representation of the "hole" in this grid. A horizontal well and 17 vertical fractures are placed in the reservoir, as shown in Fig. 27. The six "brown" fractures are directly connected to the wellbore, and their conductivity is 1000 md-ft; the "grey" fractures are not directly connected to the wellbore, and their conductivity is 10 md-ft. Other simulation parameters are summarized in Table 8. Only one hydrocarbon component is used in the simulation (C_{20}). For the water-oil two-phase flow, the same relative permeability curves as in Case 3 are used.

Fig. 28 shows the simulated oil flow rate. Fig. 29 presents the pressure profile after 10 days of production. The depleted zone around fractures can be observed in the pressure profile. Being connected to the well and having high fracture conductivity, the "brown" fractures have a major impact on the pressure distribution. On the other hand, the "grey" fractures have much less impact on the pressure distribution compared with the "brown" fractures. The pressure interference between fractures can also be observed. Furthermore, the impact of the "hole" can also be clearly seen from the pressure distribution around it. Together with Case 3, this case study shows the high flexibility of unstructured grids in representing various types of reservoir geometries, such as irregular boundaries and low-permeability zones. Because EDFM makes it easy to simulate complex fractures in such grids, the combination of unstructured gridding with the EDFM provides a convenient solution for simulating highly fractured reservoirs with complex geometries.

10. Discussions

The main goal of this work is to develop an approach that can apply the EDFM to unstructured grids using the EbFVM. The EDFM makes it relatively easy to simulate complex fractures in such grids. By combining the EDFM with unstructured gridding, the approach in this work provides high flexibility in simulating densely fractured media with complex geometries. In addition, the simulation results are insensitive to matrix gridding for long-term production forecasting, as shown in Cases 1, 2, and 4. This allows the possibility of modifying matrix grids without considering the existence of fractures. Furthermore, because of the separate gridding of the matrix and fractures, it is not necessary to re-grid the matrix after changing the fracture locations and geometries or introducing new fractures, as has been shown in Cases 1 and 2. This greatly simplifies the procedures of sensitivity studies and history matching with fractures.

Because of the complexity of the discretization in unstructured grids and the various types of elements that are being used, there are certain complexities related to the implementation of the EDFM in unstructured grids compared with that in Cartesian grids. The implementation of the approach presented in this paper requires robust geometrical algorithms to split the elements, find intersections between fractures and SCVs, and merge fracture segments. It should be noted that the unique feature of the EbFVM requires modification of the procedure to compute matrix-fracture transmissibility factors. The matrix-fracture intersection computation is conducted on the SCV level, and an additional "merging" step is necessary to reduce the number of fracture unknowns during the simulation.

As mentioned earlier, in unstructured grids, another common way of simulating fractures is to explicitly grid the fractures. Compared with this approach, the method in this paper provides high flexibility in simulating complex fractures, and it greatly simplifies the matrix-grid generation process. However, one drawback of the implementation in this paper is that it does not consider the case where fractures are acting as flow barriers. In such cases, explicit gridding needs to be used to represent these flow barriers. Also, due to the "linear pressure distribution" assumption used in the derivation of the matrix-fracture transmissibility formulation, a large error could be introduced if the pressure distribution around fractures deviates significantly from this assumption, especially in the vicinity of fractures. Another important aspect is that when explicit gridding of fractures is applied, higher-order methods could be used to reduce the influence of numerical dispersion on the

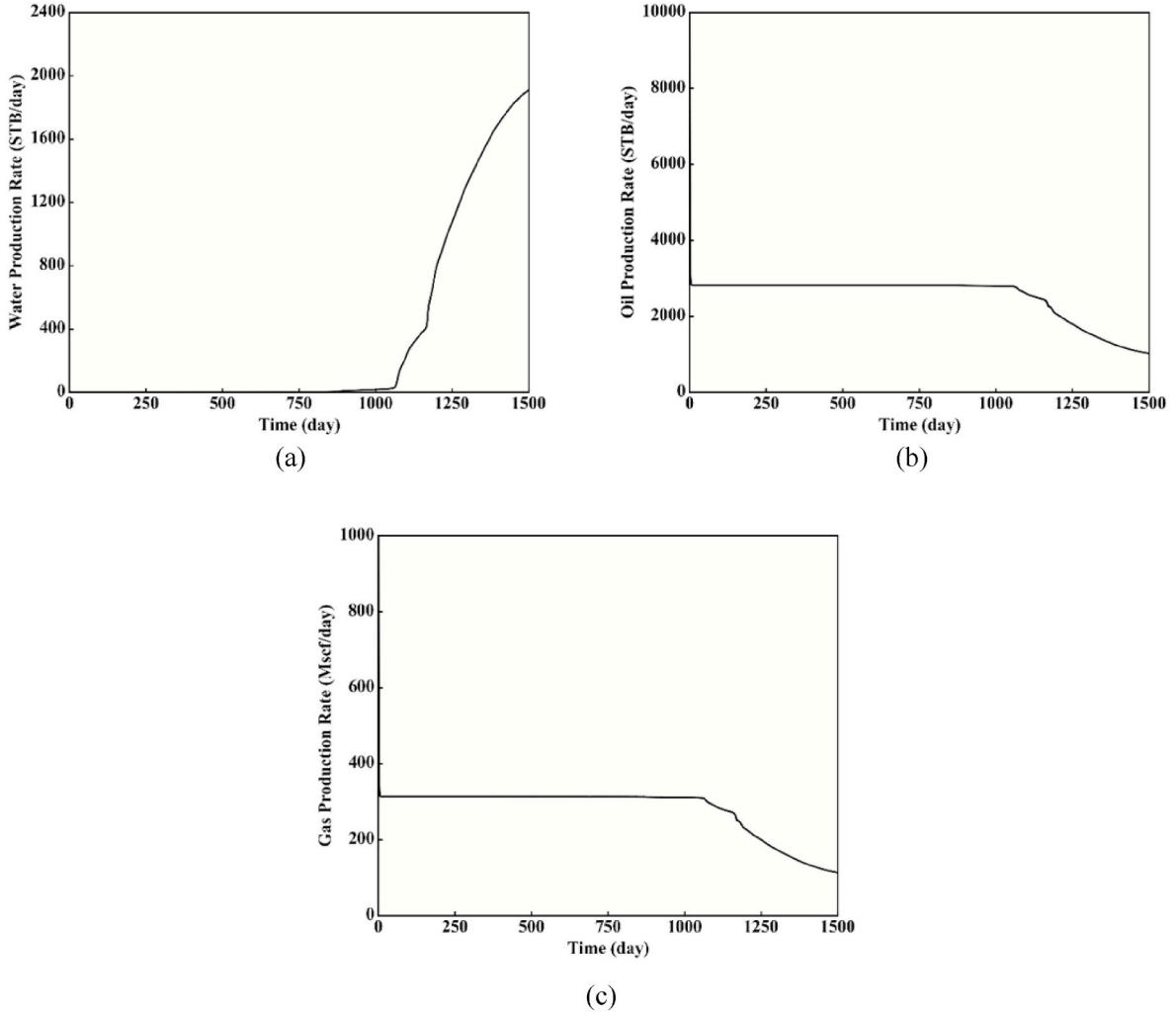

Fig. 21. Predicted (a) water, (b) oil, and (c) gas production rate in Case 3.

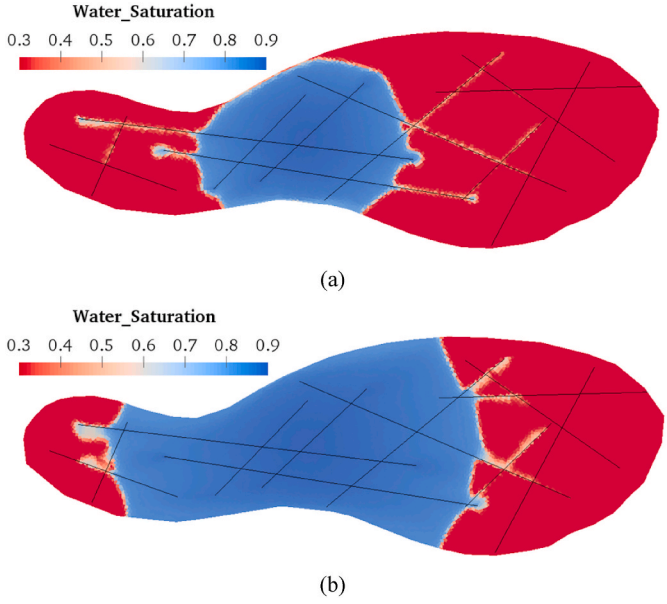

Fig. 22. Water saturation profiles after (a) 500 days and (b) 1000 days of injection in Case 3.

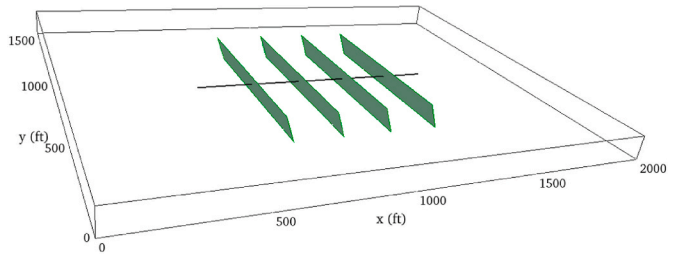

Fig. 23. Reservoir dimensions, location of well, and locations of hydraulic fractures in Case 4. The horizonal well (represented by the black line) is in the middle of the reservoir. The four green polygons represent the hydraulic fractures. The dip of the hydraulic fractures is 70°. (For interpretation of the references to color in this figure legend, the reader is referred to the Web version of this article.)

Table 6
Summary of the numbers of vertices and elements in the four grids in Case 4.

Grid	Number of vertices	Number of elements
A	30250	157464 (tetrahedron)
B	33275	58320 (prism)
C	30250	26244 (hexahedron)
D	31006	13392 (tetrahedron), 23508 (hexahedron), and 3780 (pyramid)

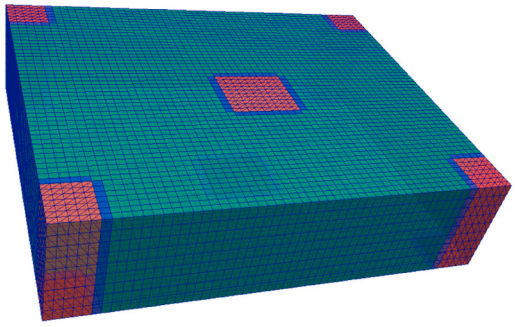

Fig. 24. Grid with mixed elements (Grid D in Table 6). The tetrahedron, hexahedron, and pyramid elements are shown in red, green, and blue, respectively. The length in the vertical direction is shown five times the real size. (For interpretation of the references to color in this figure legend, the reader is referred to the Web version of this article.)

Table 7
Key simulation parameters used in Case 4.

Parameter	Value	Unit	Parameter	Value	Unit
Reservoir permeability	0.0003	md	Initial water saturation	0.2	–
Reservoir porosity	0.1	–	Initial gas saturation	0.8	–
Initial reservoir pressure	4000	psi	Initial gas rel. perm.	0.8	–
Reservoir temperature	200	°F	Well bottomhole pressure	2000	psi
Rock compressibility	4×10^{-6}	psi^{-1}	Wellbore radius	0.25	ft
Water compressibility	3×10^{-6}	psi^{-1}			

simulation results, which has been reported in the literature (Zidane and Firoozabadi, 2018). Further development of the EDFM is required to address such issues.

It should also be noted that because the EDFM can be applied to both structured and unstructured grids, it provides a general solution for simulating fractures given a matrix grid. Therefore, it allows for high flexibility for the selection of the matrix grid type. If the geometries and subsurface features (other than fractures) of the fractured reservoir are relatively simple, which does not necessitate the usage of unstructured grids, a structured grid could be used together with the EDFM to simulate the complex fractures in the reservoir, which takes advantage of the benefits offered by structured gridding. In other cases, by using the EDFM, the process of creating the matrix grids could be largely simplified because the existence of fractures may not need to be taken into account at this stage.

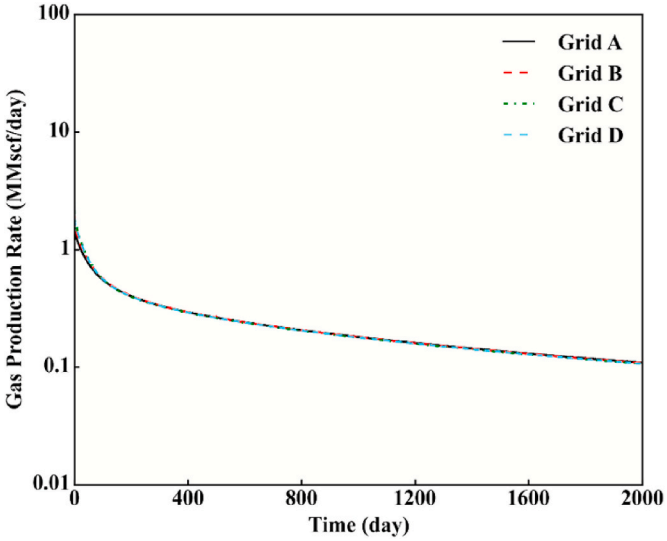

Fig. 25. Predicted surface gas production rates on the four different grids in Case 4.

11. Conclusions

In this work, a methodology was developed to apply the EDFM in 2D and 3D unstructured grids using the EbFVM. The focus of the methodology was on the discretization of fractures and the calculation of matrix-fracture transmissibility factors. The matrix-fracture intersections are computed on SCVs, and an additional merging step is added to reduce the number of fracture unknowns. In 2D grids, triangular and quadrilateral matrix elements can be used; in 3D grids, four types of matrix elements were used: tetrahedron, prism, hexahedron, and pyramid. It is also possible to have mixed elements in a single grid, which could provide more flexibility for gridding complex reservoirs. The methodology was implemented in an EDFM preprocessing code.

The methodology was demonstrated for 2D and 3D simulations in an in-house, IMPEC, compositional simulator. All types of 2D and 3D elements were involved in the simulations. Results showed that fractures can be effectively simulated with the EDFM in such grids. Furthermore, when the number of control volumes is similar, the proposed method can obtain similar results on different grids with various types of elements, assuming the same reservoir and fracture properties.

The use of unstructured grids makes it convenient to represent complex reservoir geometries, and through the EDFM, complicated gridding around fractures is avoided, and minimum adjustment is required on the original grid. Therefore, the combination of unstructured gridding with the EDFM in this work provides high flexibility for simulating densely fractured media with complex geometries.

This work also shows the high extensibility of the EDFM. It can be combined with different types of matrix gridding and numerical

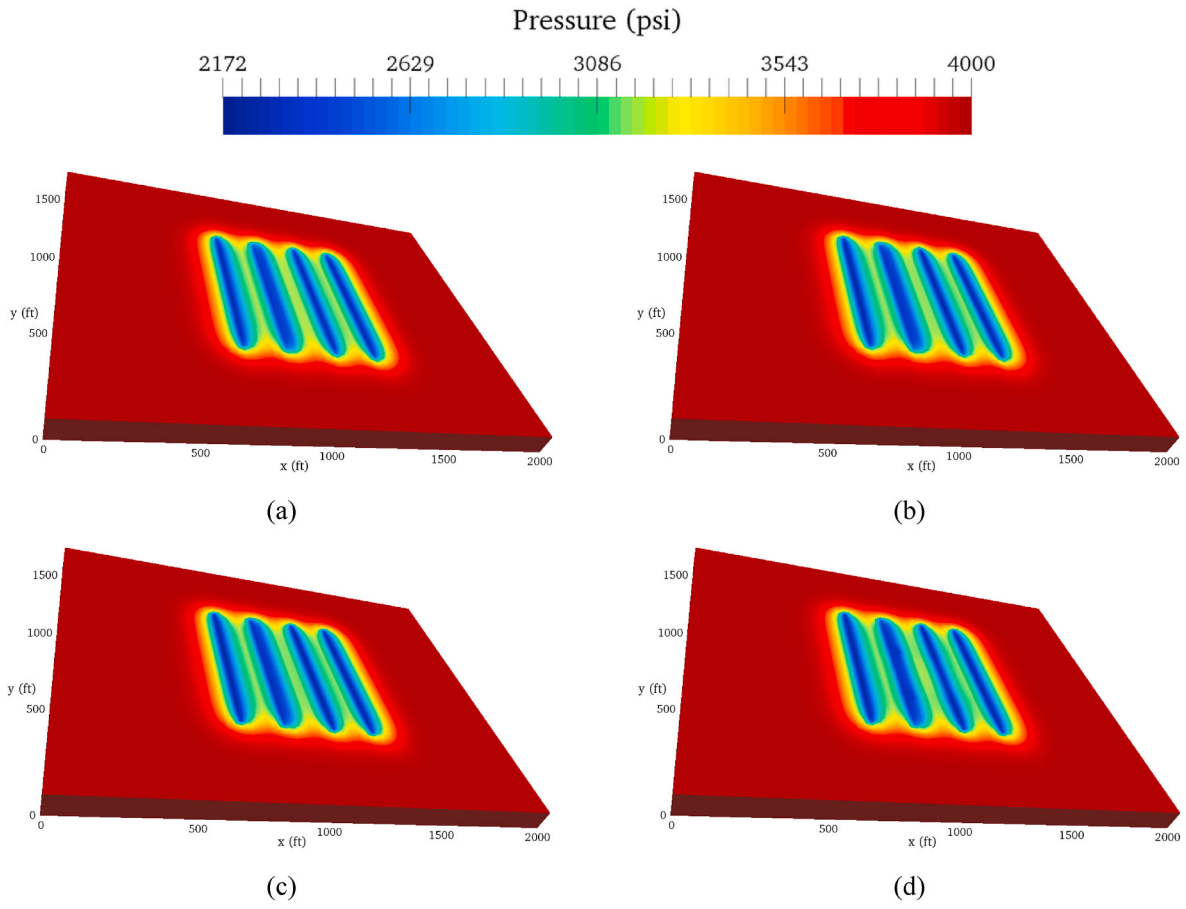

Fig. 26. Predicted pressure profiles after 1000 days of production. (a)–(d) Results using Grids A through D in Table 6.

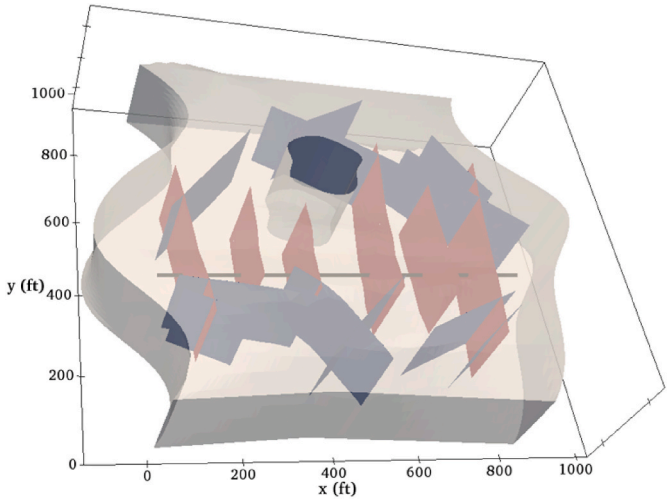

Fig. 27. Reservoir geometry, locations of fractures, and location of well in Case 5. The grey line represents the horizonal well, and the brown and grey polygons represent fractures. The "brown" fractures are directly connected to the wellbore and the "grey" fractures are not directly connected to the wellbore. (For interpretation of the references to color in this figure legend, the reader is referred to the Web version of this article.)

Table 8
Simulation parameters used in Case 5.

Parameter	Value	Unit	Parameter	Value	Unit
Horizontal permeability	0.05	md	Rock compressibility	1×10^{-6}	psi^{-1}
Vertical permeability	0.005	md	Water compressibility	1×10^{-6}	psi^{-1}
Reservoir porosity	0.3	–	Initial water saturation	0.3	–
Initial reservoir pressure	3000	psi	Well bottomhole pressure	2000	psi
Reservoir temperature	160	°F	Wellbore radius	0.5	ft

formulations. Overall, it serves as a general method to model fractures in reservoir simulation.

CRediT authorship contribution statement

Y. Xu: Writing - original draft, Methodology, Software, Visualization, Validation. **I.C.M. Lima:** Methodology, Software, Data curation. **F. Marcondes:** Methodology, Investigation, Writing - review & editing. **K. Sepehrnoori:** Conceptualization, Supervision, Writing - review & editing.

Declaration of competing interest

The authors declare that they have no known competing financial interests or personal relationships that could have appeared to influence the work reported in this paper.

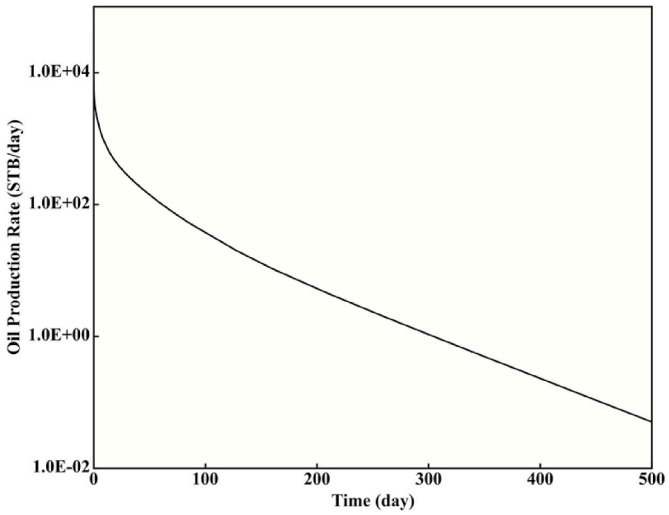

Fig. 28. Predicted surface oil production rate.

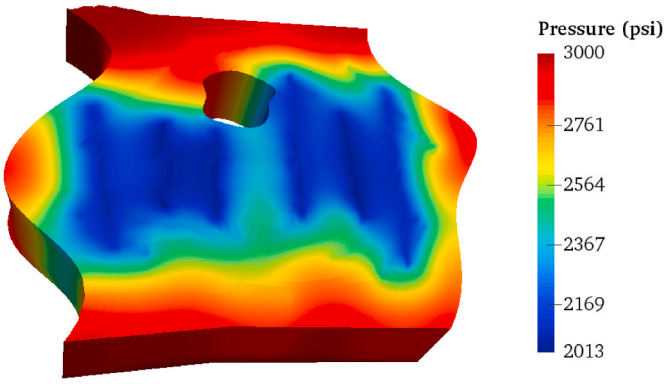

Fig. 29. Predicted pressure profile at 10 days.

SI Metric Conversion Factors

Cp	× 1.0*	E−03	=	Pa·s
Day	× 8.64	E+04	=	S
Ft	× 3.048	E−01	=	M
°F	(°F-32)/1.8		=	°C
°F	(°F+459.67)/1.8		=	K
lb/ft^3	× 1.6018	E+01	=	kg/m^3
Md	× 9.869	E−16	=	m^2
Psi	× 6894.757	E+00	=	kPa
Scf	× 2.831	E−02	=	m^3
STB	× 1.5899	E−01	=	m^3
Ton	× 9.072	E+02	=	kg

Appendix A. Shape Functions for Two-Dimensional and Three-Dimensional Elements

The shape function N_i is defined for each type of element. In 2D grids, triangular and quadrilateral elements are used. Figure A.1 and Figure A.2 show the definition of local coordinates (ξ, η) in triangular and quadrilateral elements, respectively. The shape functions for a triangular element are

$$\begin{aligned} N_1(\xi,\eta) &= 1-\xi-\eta; \\ N_2(\xi,\eta) &= \xi; \\ N_3(\xi,\eta) &= \eta. \end{aligned} \tag{A-1}$$

The shape functions for a quadrilateral element are

$$
\begin{aligned}
N_1(\xi,\eta) &= \frac{1}{4}(1-\xi)(1-\eta);\\
N_2(\xi,\eta) &= \frac{1}{4}(1+\xi)(1-\eta);\\
N_3(\xi,\eta) &= \frac{1}{4}(1+\xi)(1+\eta);\\
N_4(\xi,\eta) &= \frac{1}{4}(1-\xi)(1+\eta).
\end{aligned}
\tag{A-2}
$$

In 3D grids, four types of elements can be used: tetrahedron, prism, hexahedron, and pyramid. The definition of local coordinates (ξ,η,γ) in 3D elements is presented in Figure A.2. The shape functions for a tetrahedron element are

$$
\begin{aligned}
&N_1(\xi,\eta,\gamma) = 1-\xi-\eta-\gamma;\\
&N_2(\xi,\eta,\gamma) = \xi;\\
&N_3(\xi,\eta,\gamma) = \eta;\\
&N_4(\xi,\eta,\gamma) = \gamma.
\end{aligned}
\tag{A-3}
$$

The shape functions for a prism element are

$$
\begin{aligned}
&N_1(\xi,\eta,\gamma) = (1-\xi-\eta)(1-\gamma);\\
&N_2(\xi,\eta,\gamma) = \xi(1-\gamma);\\
&N_3(\xi,\eta,\gamma) = \eta(1-\gamma);\\
&N_4(\xi,\eta,\gamma) = \gamma(1-\xi-\eta);\\
&N_5(\xi,\eta,\gamma) = \xi\gamma;\\
&N_6(\xi,\eta,\gamma) = \eta\gamma.
\end{aligned}
\tag{A-4}
$$

The shape functions for a hexahedron element are

$$
\begin{aligned}
N_1(\xi,\eta,\gamma) &= \frac{1}{8}(1+\xi)(1-\eta)(1+\gamma);\\
N_2(\xi,\eta,\gamma) &= \frac{1}{8}(1+\xi)(1-\eta)(1-\gamma);\\
N_3(\xi,\eta,\gamma) &= \frac{1}{8}(1-\xi)(1-\eta)(1-\gamma);\\
N_4(\xi,\eta,\gamma) &= \frac{1}{8}(1-\xi)(1-\eta)(1+\gamma);\\
N_5(\xi,\eta,\gamma) &= \frac{1}{8}(1+\xi)(1+\eta)(1+\gamma);\\
N_6(\xi,\eta,\gamma) &= \frac{1}{8}(1+\xi)(1+\eta)(1-\gamma);\\
N_7(\xi,\eta,\gamma) &= \frac{1}{8}(1-\xi)(1+\eta)(1-\gamma);\\
N_8(\xi,\eta,\gamma) &= \frac{1}{8}(1-\xi)(1+\eta)(1+\gamma).
\end{aligned}
\tag{A-5}
$$

The shape functions for a pyramid element are

$$
\begin{aligned}
N_1(\xi,\eta,\gamma) &= \frac{1}{4}[(1-\xi)(1-\eta)-\gamma+\xi\eta\gamma/(1-\gamma)];\\
N_2(\xi,\eta,\gamma) &= \frac{1}{4}[(1+\xi)(1-\eta)-\gamma-\xi\eta\gamma/(1-\gamma)];\\
N_3(\xi,\eta,\gamma) &= \frac{1}{4}[(1+\xi)(1+\eta)-\gamma+\xi\eta\gamma/(1-\gamma)];\\
N_4(\xi,\eta,\gamma) &= \frac{1}{4}[(1-\xi)(1+\eta)-\gamma-\xi\eta\gamma/(1-\gamma)];\\
N_5(\xi,\eta,\gamma) &= \gamma.
\end{aligned}
\tag{A-6}
$$

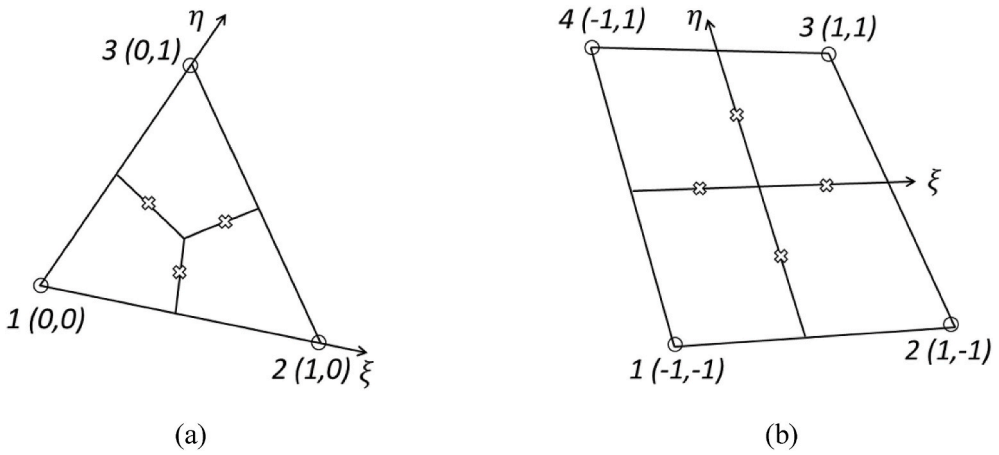

Fig. A.1. Definition of local coordinates in 2D elements. (a) Triangular element. (b) Quadrilateral element. For each vertex, its index and (ξ, η) coordinates are shown. The integration points in the elements are also shown.

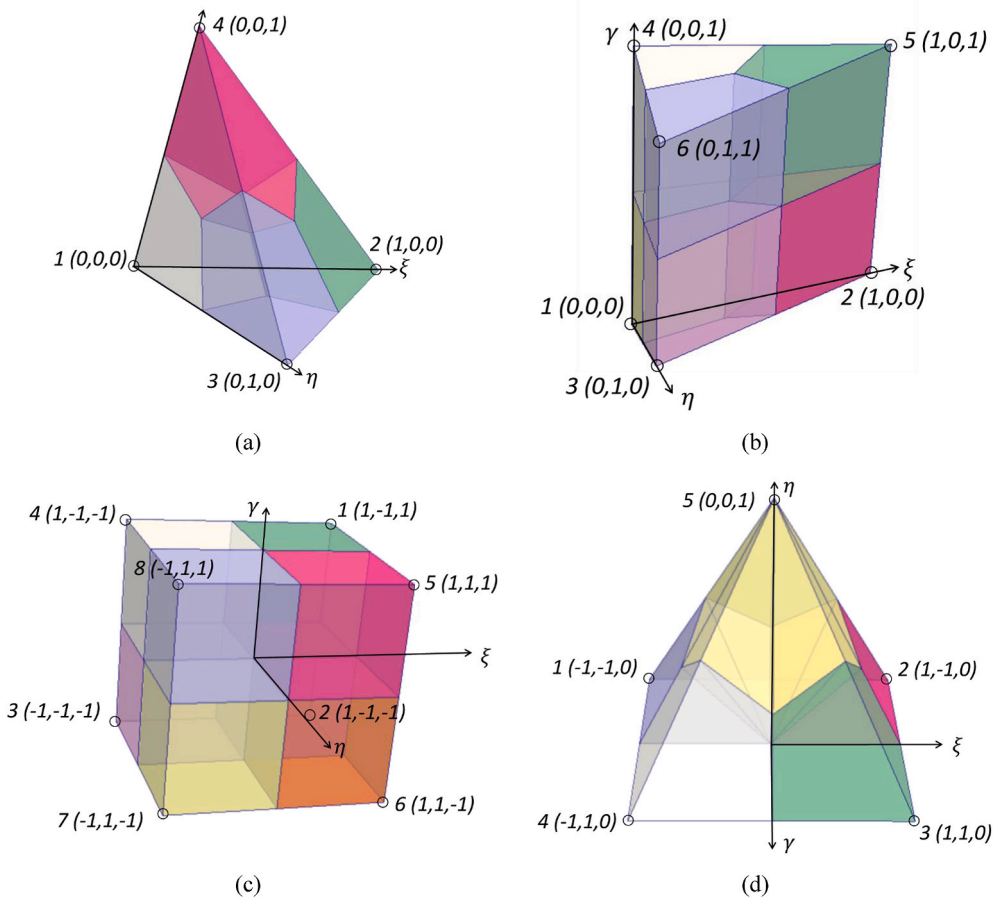

Fig. A.2. Definition of local coordinates in 3D elements. (a) Tetrahedron element. (b) Prism element. (c) Hexahedron element. (d) Pyramid element. For each vertex, its index and (ξ, η, γ) coordinates are shown.

Nomenclature

$A_{f,SCV}$	area of fracture, ft^2
$\overrightarrow{A_l}$	area of interface between sub-control volumes, ft^2
d	distance, ft
F_k	molar flow rate of component k, mole/day
k_{rj}	relative permeability of phase j
$\overrightarrow{\overrightarrow{K}}$	permeability tensor, md
$\overrightarrow{n}$	unit normal vector

n_c	number of hydrocarbon components
n_{ip}	number of integration points
n_{merge}	number of initial fracture segments to merge
n_p	number of phases
N_i	shape function of vertex i
N_k	number of moles of component k, mole
n_v	number of vertices in grid
N_v	number of vertices of an element
S_w	water saturation
t	time, day
T	transmissibility factor, md-ft
q_k	injection/production molar rate of component k from wells, mole/day
x	Cartesian coordinate, ft
x_{kj}	mole fraction of component k in phase j
y	Cartesian coordinate, ft
z	Cartesian coordinate, ft
Φ	physical property value at a point inside an element
$\vec{\nabla}\Phi_{jl}$	flow potential gradient in phase j at the lth integration point, psi/ft
ξ	local coordinate
ξ_j	the molar density of phase j
η	local coordinate
γ	local coordinate
μ_j	viscosity of phase j, cp

Appendix B. Supplementary data

Supplementary data to this article can be found online at https://doi.org/10.1016/j.petrol.2020.107725.

References

Araújo, A.L.S., Fernandes, B.R.B., Drumond Filho, E.P., et al., 2016. 3D compositional reservoir simulation in conjunction with unstructured grids. Braz. J. Chem. Eng. 33 (2), 347–360.

Baliga, B.R., Patankar, S.V., 1980. A new finite-element formulation for convection-diffusion problems. Numer. Heat Tran. 3 (4), 393–409.

Chai, Z., Tang, H., He, Y., et al., 2018. Uncertainty quantification of the fracture network with a novel fractured reservoir forward model. In: Presented at the SPE Annual Technical Conference and Exhibition, Dallas, Texas, 24-26 September. SPE-191395-MS. https://doi.org/10.2118/191395-MS.

Cordazzo, J., Maliska, C., da Silva, A.F.C., et al., 2005. An element based conservative scheme using unstructured grids for reservoir simulation. In: Presented at the 18th World Petroleum Congress, Johannesburg, South Africa, 25-29 September.

Ding, D.Y., Farah, N., Bourbiaux, B., et al., 2018. Simulation of matrix/fracture interaction in low-permeability fractured unconventional reservoirs. SPE J. 23 (4) https://doi.org/10.2118/182608-PA, 1,389-1,411. SPE-182608-PA.

Du, S., Liang, B., Yuanbo, L., 2017. Field study: embedded discrete fracture modeling with artificial intelligence in permian basin for shale formation. In: Presented at the SPE Annual Technical Conference and Exhibition, San Antonio, Texas, 9-11 October.

Durlofsky, L.J., Chien, M.C.H., 1993. Development of a mixed finite-element based compositional reservoir simulator. In: Presented at the SPE Symposium on Reservoir Simulation, New Orleans, Louisiana, 28 February-3 March. SPE-25253-MS. https://doi.org/10.2118/25253-MS.

Edwards, M.G., 2002. Unstructured, control-volume distributed, full-tensor finite-volume schemes with flow based grids. Comput. Geosci. 6 (2002), 433–452.

Fang, S., Cheng, L., Huang, S., et al., 2016. Laplace domain coupled dual continuum and embedded discrete fracture model for rate transient analysis in low permeability reservoirs. In: Presented at the SPE Low Perm Symposium, Denver, Colorado, 5-6 May. SPE-180265-MS. https://doi.org/10.2118/180265-MS.

Fernandes, B.R.B., Marcondes, F., Sepehrnoori, K., 2016. Comparison of two volume balance fully implicit approaches in conjunction with unstructured grids for compositional reservoir simulation. Appl. Math. Model. 40 (2016), 5,153-155,170.

Fernandes, B.R.B., Lima, I.D., Drumond Filho, E.P., et al., 2017. A TVD scheme for 3d unstructured grids applied to compositional reservoir simulation. Braz. J. Chem. Eng. 34 (4), 1161–1174.

Flemisch, B., Berre, I., Boon, W., et al., 2018. Benchmarks for single-phase flow in fractured porous media. Adv. Water Resour. 111 (2018), 239–258.

Forsyth, P.A., 1990. A control-volume, finite-element method for local mesh refinement in thermal reservoir simulation. SPE Reservoir Eng. 5 (4), 561–566. https://doi.org/10.2118/18415-PA. SPE-18415-PA.

Fumagalli, A., Pasquale, L., Zonca, S., et al., 2016. An upscaling procedure for fractured reservoirs with embedded grids. Water Resour. Res. 52 (8), 6506–6525. https://doi.org/10.1002/2015WR017729.

Fung, L.S.-K., Hiebert, A.D., Nghiem, L.X., 1992. Reservoir simulation with a control-volume finite-element method. SPE Reservoir Eng. 7 (3), 349–357. https://doi.org/10.2118/21224-PA. SPE-21224-PA.

Hearn, C.L., Al-Emadi, I.A.A., Worley, P.L.H., et al., 1997. Improved oil recovery in a tight reservoir with conductive faults, ISND shuaiba, Qatar. In: Presented at the SPE Annual Technical Conference and Exhibition, San Antonio, Texas, 5-8 October. https://doi.org/10.2118/38908-MS. SPE-38908-MS.

Hoteit, H., Firoozabadi, A., 2006. Compositional modeling by the combined discontinuous galerkin and mixed methods. SPE J. 11 (1), 19–34. https://doi.org/10.2118/90276-PA. SPE-90276-PA.

Hui, M.-H., Karimi-Fard, M., Mallison, B., et al., 2018. A general modeling framework for simulating complex recovery processes in fractured reservoirs at different resolutions. SPE J. 23 (2), 598–613. https://doi.org/10.2118/182621-PA. SPE-182621-PA.

Hui, M.-H., Dufour, G., Vitel, S., et al., 2019. A robust embedded discrete fracture modeling workflow for simulating complex processes in field-scale fractured reservoirs. In: Presented at the SPE Reservoir Simulation Conference, Galveston, Texas, 10-11 April. https://doi.org/10.2118/193827-MS. SPE-193827-MS.

Jiang, J., Younis, R.M., 2016. Hybrid coupled discrete-fracture/matrix and multicontinuum models for unconventional-reservoir simulation. SPE J. 21 (3), 1,009–1,027. https://doi.org/10.2118/178430-PA. SPE-178430-PA.

Jiang, J., Younis, R.M., 2017. An improved projection-based embedded discrete fracture model (pedfm) for multiphase flow in fractured reservoirs. Adv. Water Resour. 109 (2017), 267–289.

Karimi-Fard, M., Durlofsky, L.J., 2016. A general gridding, discretization, and coarsening methodology for modeling flow in porous formations with discrete geological features. Adv. Water Resour. 96 (2016), 354–372.

Karimi-Fard, M., Durlofsky, L.J., Aziz, K., 2004. An efficient discrete-fracture model applicable for general-purpose reservoir simulators. SPE J. 9 (2), 227–236. https://doi.org/10.2118/88812-PA. SPE-88812-PA.

Lee, S.H., Lough, M.F., Jensen, C.L., 2001. Hierarchical modeling of flow in naturally fractured formations with multiple length scales. Water Resour. Res. 37 (3), 443–455. https://doi.org/10.1029/2000WR900340.

Li, L., Lee, S.H., 2008. Efficient field-scale simulation of black oil in a naturally fractured reservoir through discrete fracture networks and homogenized media. SPE Reservoir Eval. Eng. 11 (4), 750–758. https://doi.org/10.2118/103901-PA. SPE-103901-PA.

Maliska, C.R., 2004. Computational Heat Transfer and Fluid Mechanics, second ed. Editora LTC, Florianopolis.

Marcondes, F., Sepehrnoori, K., 2007. Unstructured grids and an element-based conservative approach for compositional reservoir simulation. In: Presentation at the 19th International Congress of Mechanical Engineering, Brasilia, Brazil, November 5-9.

Marcondes, F., Sepehrnoori, K., 2010. An element-based finite-volume method approach for heterogeneous and anisotropic compositional reservoir simulation. J. Petrol. Sci. Eng. 73 (2010), 99–106.

Marcondes, F., Santos, L.O.S., Varavei, A., et al., 2013. A 3D hybrid element-based finite-volume method for heterogeneous and anisotropic compositional reservoir simulation. J. Petrol. Sci. Eng. 108 (2013), 342–351.

Matthai, S., Menzentsev, A., Belayneh, M., 2005. Control-volume finite-element two phase flow experiments with fractured rock represented by unstructured 3D hybrid meshes. In: Presented at the SPE Reservoir Simulation Symposium, the Woodlands, Texas, 31 January-2 February. https://doi.org/10.2118/93341-MS. SPE-93341-MS.

Moinfar, A., Varavei, A., Sepehrnoori, K., et al., 2013. Development of a coupled dual continuum and discrete fracture model for the simulation of unconventional reservoirs. In: Presented at the SPE Reservoir Simulation Symposium, the Woodlands, Texas, 18-20 February. https://doi.org/10.2118/163647-MS. SPE-163647-MS.

Moinfar, A., Varavei, A., Sepehrnoori, K., et al., 2014. Development of an efficient embedded discrete fracture model for 3D compositional reservoir simulation in fractured reservoirs. SPE J. 19 (2), 289–303. https://doi.org/10.2118/154246-PA. SPE-154246-PA.

Noorishad, J., Mehran, M., 1982. An upstream finite element method for solution of transient transport equation in fractured porous media. Water Resour. Res. 18 (3), 588–596. https://doi.org/10.1029/WR018i003p00588.

Norbeck, J.H., McClure, M.W., Lo, J.W., et al., 2016. An embedded fracture modeling framework for simulation of hydraulic fracturing and shear stimulation. Comput. Geosci. 20 (1), 1–18.

Panfili, P., Cominelli, A., 2014. Simulation of miscible gas injection in a fractured carbonate reservoir using an embedded discrete fracture model. In: Presented at the Abu Dhabi International Petroleum Exhibition and Conference, Abu Dhabi, 10-13 November. https://doi.org/10.2118/171830-MS. SPE-171830-MS.

Panfili, P., Colin, R., Cominelli, A., et al., 2015. Efficient and effective field scale simulation of hydraulic fractured wells: methodology and application. In: Presented at the SPE Reservoir Characterisation and Simulation Conference and Exhibition, Abu Dhabi, UAE, 14-16 September. https://doi.org/10.2118/175542-MS. SPE-175542-MS.

Philip, Z.G., Jennings, J.W., Olson, J.E., et al., 2005. Modeling coupled fracture-matrix fluid flow in geomechanically simulated fracture networks. SPE Reservoir Eval. Eng. 8 (4), 300–309. https://doi.org/10.2118/77340-PA. SPE-77340-PA.

Prévost, M., Edwards, M.G., Blunt, M.J., 2002. Streamline tracing on curvilinear structured and unstructured grids. SPE J. 7 (2), 139–148. https://doi.org/10.2118/78663-PA. SPE-78663-PA.

Prévost, M., Lepage, F., Durlofsky, L.J., et al., 2005. Unstructured 3D gridding and upscaling for coarse modelling of geometrically complex reservoirs. Petrol. Geosci. 11 (4), 339–345.

Samier, P., Masson, R., 2017. Implementation of a vertex-centered method inside an industrial reservoir simulator: practical issues and comprehensive comparison with corner-point grids and perpendicular-bisector-grid models on a field case. SPE J. 22 (2), 660–678. https://doi.org/10.2118/173309-PA. SPE-173309-PA.

Santos, L.O.S., Marcondes, F., Sepehrnoori, K., 2013. A 3D compositional miscible gas flooding simulator with dispersion using element-based finite-volume method. J. Petrol. Sci. Eng. 112 (2013), 61–68. https://doi.org/10.1016/j.petrol.2013.10.004.

Tene, M., Bosma, S.B., Al Kobaisi, M.S., et al., 2017. Projection-based embedded discrete fracture model. Adv. Water Resour. 105 (2017), 205–216.

Verma, S., Aziz, K., 1997. A control volume scheme for flexible grids in reservoir simulation. In: Presented at the SPE Reservoir Simulation Symposium, Dallas, Texas, 8-11 June. https://doi.org/10.2118/37999-MS. SPE-37999-MS.

Vitel, S., Souche, L., 2007. Unstructured upgridding and transmissibility upscaling for preferential flow paths in 3D fractured reservoirs. In: Presented at the SPE Reservoir Simulation Symposium, Houston, Texas, U.S.A., 26-28 February. SPE-106483-MS. https://doi.org/10.2118/106483-MS.

Xu, Y., Sepehrnoori, K., 2019. Development of an embedded discrete fracture model for field-scale reservoir simulation with complex corner-point grids. SPE J. SPE-195572-PA (accepted, (in press) soon).

Xu, Y., Cavalcante Filho, J.S.A., Yu, W., et al., 2017. Discrete-fracture modeling of complex hydraulic-fracture geometries in reservoir simulators. SPE Reservoir Eval. Eng. 20 (2), 403–422. https://doi.org/10.2118/183647-PA. SPE-183647-PA.

Yang, D., Xue, X., Chen, J., 2018. High resolution hydraulic fracture network modeling using flexible dual porosity dual permeability framework. In: Presented at the SPE Western Regional Meeting, Garden Grove, California, 22-26 April. SPE-190096-MS. https://doi.org/10.2118/190096-MS.

Zidane, A., Firoozabadi, A., 2018. Efficient simulation of two-phase compositional flow in fractured reservoirs using 3D unstructured gridding in complex geometries. In: Presented at the SPE Annual Technical Conference and Exhibition, Dallas, Texas. https://doi.org/10.2118/191405-MS.